

Numerical simulation of bubble deformation and breakup under simple linear shear flows

Mitsuhiko Ohta^{a,b,*}, Tetsuya Ueta^b, Yozo Toei^c, Edwin Jimenez^d, Mark Sussman^e

^a*Department of Mechanical Science, Graduate School of Technology, Industrial and Social Sciences, Tokushima University, 2-1 Minamijyousanjima-cho, Tokushima 770-8506, Japan*

^b*Department of Mechanical Engineering, Graduate School of Technology, Industrial and Social Sciences, Tokushima University, 2-1 Minamijyousanjima-cho, Tokushima 770-8506, Japan*

^c*High Performance Plastics Company, Sekisui Chemical Co., Ltd., 2-1 Hyakuyama, Mishimagun Shimamoto-cho, Osaka 618-0021, Japan*

^d*Spectral Numerical, LLC, 1942 Broadway St., STE 314C, Boulder, CO 80302, USA*

^e*Department of Mathematics, Florida State University, Tallahassee, FL 32306, USA*

Abstract

Numerical simulations are presented for the deformation and breakup of a bubble in liquids undergoing simple linear shear flow in a variety of regimes including the low Capillary number, high Reynolds number regime. Numerical results are obtained using a projection method for incompressible two-phase flow. The method represents interfaces using the sharp interface coupled level set and Volume-Of-Fluid (CLSVOF) method. To verify the CLSVOF numerical algorithm and provide a basis for comparison, computational results are also presented that compare with previous, more popular, drop deformation and rupture simulations. The numerical results reveal that the shear-induced bubble deformation and breakup process differs significantly from that of the analogous drop system under similar flow conditions. The first distinguishing factor for bubble breakup is that the magnitude of shear flow necessary for causing rupture is much larger than that in the drop system case. In other words, a larger Reynolds number is needed to induce bubble breakup. The second distinct feature of the bubble system versus the drop system is that the bubble does not maintain a stable deformed shape as the system parameters approach the critical “breakup” Reynolds number. It is asserted that the differences in morphology for a bubble undergoing breakup versus a drop in the same process can be attributed to the density and viscosity ratio of the corresponding two-phase flow systems. The critical conditions for bubble breakup with respect to the Reynolds and capillary numbers are determined for several cases.

Keywords: Bubble deformation, bubble breakup, shear flow, CFD

*Corresponding author: m-ohta@tokushima-u.ac.jp

1 **1. Introduction**

2 Bubble dynamics in shear flow, including breakup, is critically important
3 for various gas-liquid scientific and engineering processes. We refer the reader
4 to the following experimental studies relating to bubble deformation in foaming
5 processes, microfluidic devices, microbubbles in the blood circulation system,
6 materials processing, pharmaceuticals, minerals engineering, bubble column re-
7 actor, underwater projectiles, polyethylene devolatilization, microfluidics, food
8 aeration, passive cyclonic separators, and cosmetics[7, 36, 4, 11, 12, 67, 13, 71,
9 5, 17, 70, 15, 16, 35, 52, 51, 21, 54]. In particular, it is the study of bubble de-
10 formation as it pertains to high-performance plastics applications that motivate
11 this work.

12 This article presents computational studies of shear-driven deformation and
13 breakup of a bubble in insoluble viscous liquids. Studying bubble break-up,
14 in which we focus only on the balance of the wall driving force and bubble
15 surface tension force, via computation rather than experiments simplifies the
16 process of setting a combination of precise, simple shear flow conditions, low
17 Capillary number ($Ca = \mu_m U / \sigma$) conditions, high Reynolds' number conditions
18 ($Re = \rho_m R U / \mu_m$), low-density ratio, low viscosity ratios, and zero buoyancy ef-
19 fects. We remark that previous controlled experimental studies on shear-driven
20 bubble deformation are restricted to the low Reynolds' number and large capil-
21 lary number regime[50, 5]. One reason is that buoyancy effects are minimized in
22 highly viscous liquids. On the other hand, many applications are characterized
23 by liquids in the high Reynolds' number regime. The physical properties that
24 distinguish bubble and drop studies are expressed in terms of the density ratio
25 $\lambda = \rho_b / \rho_m$ and the viscosity ratio $\eta = \mu_b / \mu_m$, where ρ is the fluid density, μ is
26 the viscosity and the subscripts "b" and "m" denote the "bubble" or "drop" and
27 the "matrix fluid", respectively. For a bubble in an insoluble, viscous liquid,
28 $\lambda \simeq 0$ and $\eta \simeq 0$, whereas most studies dealing with a drop in an immiscible
29 viscous liquid take $\lambda = 1$ and $\eta \simeq 1$.

30 In this work, we focus on identifying critical flow states numerically, in terms
31 of dimensionless quantities, that specify the extreme conditions at which a bub-
32 ble in shear flow first transitions from deformation to breakup. We validate our
33 numerical method by examining the sensitivity of the critical bubble deforma-
34 tion and break-up flow states with respect to the grid size. We also compare
35 with previous experimental results where the experimental data is available (the
36 high Capillary number low Reynolds' number regime). An advantage of study-
37 ing shear-driven bubble deformation and breakup computationally rather than
38 experimentally is that we can easily modify bubble/drop shape initial conditions
39 [39], the gravity force term, fluid physical properties, and the geometry of the
40 (virtual) apparatus. In our computations, the time-evolution of the boundary
41 between gas and liquid is tracked with a Coupled-Level-Set and Volume-Of-
42 Fluid (CLSVOF) sharp interface capturing algorithm [59, 61]. The rationale
43 for the CLSVOF method is that the hybrid method represents the (complex)
44 gas-liquid interfaces with minimal volume loss (property of the Volume-Of-Fluid
45 method) and minimal error in the approximation of the surface tension force

46 (property of the Level-Set method). Our sharp interface approach[61, 57, 27]
47 enables us to simulate multiphase flows without artificially giving the interface
48 an empirical thickness.

49 We focus on determining critical physical conditions in which the breakup of
50 a bubble occurs in shear flow because it is important to identify the parameter
51 regimes in which a relatively simple system transitions from stable to unstable.
52 Specifically, we ascertain the critical Reynolds number (Re_c) corresponding to
53 the bubble breakup onset condition as a function of Ca .

54 In previous experimental or computational studies on the motion of bubble
55 deformation in a simple shear flow [5, 50, 36], only findings for bubble deforma-
56 tion under very low Re number conditions ($Re \ll 1$) have been reported.
57 This is understandable since a low Reynolds number matrix fluid mitigates the
58 effect of gravity on distorting the comparison with the drop case. In the results
59 reported in [5], the $x - z$ cross section of the deforming bubble was close to
60 circular in their experiments. Also in the experiments in [5], the $x - z$ cross
61 section shows minimal overall bubble rise speed in the (very) viscous fluid in
62 comparison to the rate that the bubble deforms in the $y - z$ cross section. This
63 is expected since the experiments designed by [5] closely followed the following
64 basic assumptions: (i) “steady creeping flow with negligible inertial effects,” (ii)
65 “Incompressible Newtonian fluids,” (iii) “No buoyancy effects,” (iv) “No wall
66 effects.” In this work, we determine, for the first time, the critical Reynolds
67 number ($Re \gg 1$) that leads to bubble breakup. Additionally, our computa-
68 tional studies reveal characteristics that distinguish a drop’s deformation and
69 breakup processes versus those of a bubble.

70 We remark that there have been a number of computational articles on
71 the study of lift of slightly deformable bubbles[14, 31]. We reiterate, though,
72 that for bubble deformation and breakup in shear flows, only a few articles
73 exist: [69, 68, 53]. These previous studies mainly examined the dynamics (e.g.,
74 rotation angle) of bubble deformation in shear flow. Concerning bubble breakup,
75 Wei et al. [69] presented one numerical result for a bubble breakup process
76 under the condition of Ca (capillary number) = 35. Sharifi et al[53] presented
77 two results for bubble breakup corresponding to $Ca = 7.5$ and $Ca = 11.2$. We
78 point out that all of the previous computational research on bubble deformation
79 (and breakup) under shear driven flow[69, 68, 53] use the (explicit) Lattice
80 Boltzmann method. For accurately computing the tensile strength of a bubble,
81 and accurately computing threshold parameters for break-up (what we do in this
82 article, and what was not done in previous work), it is critical that a numerical
83 method directly enforces the velocity continuity condition and the gas-liquid
84 interface normal jump conditions. We contend that a projection method (i.e.
85 this paper and [73, 74, 41]) is the more appropriate (albeit slower) method for
86 our study rather than the Lattice Boltzmann method. Also, in contrast to the
87 Lattice Boltzmann method, our interface “capturing” method, the CLSVOF
88 method[59, 61], maintains the gas/liquid interface as sharp, enables accurate
89 approximation of the surface tension force, and by construction the CLSVOF
90 method preserves mass and volume within a fraction of a percent. The results
91 that we present in this article (see e.g. section 3.3.2) regarding measuring the

tensile strength of a bubble are unique and validated with respect to comparisons with previous experimental data (where available) and grid refinement studies. Admittably, each simulation on the finest resolution takes over a half a year to complete on a workstation because of the following unavoidable factors: (i) the large density-ratio projection method requires the solution of a large sparse, ill-conditioned, matrix system at each time step, (ii) the finer the mesh, the more precise the measured threshold, and right at the threshold (Taylor Deformation parameter $D \approx 1!$), oscillatory behaviour is observed delaying the determination of breakup or not. Finally, the larger the deformation parameter D , the longer one must make the computational domain (and thereby leading to larger domain aspect ratio) thereby adversely effecting the condition number even more for carrying our the pressure projection.

To highlight the mechanisms of bubble deformation and breakup in a shear flow, we juxtapose the bubble results with those of a drop. We remark that while the study of critical tensile strength parameters for the bubble is sparse, there have been many studies for the simpler drop problem. This is because the density ratio for the drop deformation case is almost one so that it is not required that the continuous phase liquid be highly viscous in order to mitigate buoyancy effects. For completeness, we give a brief overview of previous “tensile strength” studies pertaining to drops.

The study of the deformation and breakup of a drop in immiscible viscous liquids undergoing simple linear shear flow has been investigated extensively due to its fundamental importance to emulsion processes, materials processing, mixing, and reaction devices. The pioneering experimental work on this problem was performed by Taylor in the early 1930s [64, 65], and the subsequent theoretical and experimental progress up to the 1980s and 1990s was reviewed in [43] and [56], respectively. By the 2000s, progress in computational fluid dynamics (CFD) techniques and increased access to powerful computing resources led to a surge of research focused on direct simulations of this problem. In particular, detailed computational investigations of drop breakup, based on a Volume-of-Fluid (VOF) method [20] were presented in [33, 47, 49, 48, 28, 44, 45, 46]. Since then, the literature on computational studies on the deformation and breakup of a single or several drops in shear flow has continued to grow [9, 23, 72, 3, 25, 10, 29, 30, 24, 19, 1, 75] and a variety of numerical techniques have been developed to tackle this problem, including boundary-integral approaches [8, 26], lattice Boltzmann methods [22, 29], front tracking schemes [66], and interface-capturing level set methods [60].

Thus, a lot of studies about the deformation and breakup of a drop in simple linear shear have been presented so far. In contrast, few studies have been conducted on bubble deformation and breakup. In the low Capillary number, high Reynolds’ number regime, there are no controlled experiments or simulations. We reiterate why there have been few studies regarding the “tensile strength” of bubbles. Experimentally, if one wants to isolate the interplay of shearing force with the bubble surface tension force, in the moderate to high Reynolds number regime, and low Capillary number regime, one is restricted to microgravity conditions. Computational experiments are difficult too. In

138 order to accurately compute the tensile strength of a bubble, one must resort
 139 to a combination of parallel computing, the multigrid preconditioned conjugate
 140 gradient method[63, 61] for poorly conditioned large sparse matrix systems,
 141 adaptive mesh refinement[76, 61], and a robust, volume preserving interface
 142 tracking method (we use the CLSVOF method[59, 61]). These aspects of our
 143 algorithm allow one to accurately simulate the balance of the restoring bubble
 144 surface tension force against the driving wall shear force.

145 2. Problem Description

146 Figure 1(a) shows a schematic of the computational system for our studies
 147 of a bubble (or drop) in shear flow. The computational domain consists of a
 148 three-dimensional rectangular domain with the dimensions of L (length) $\times W$
 149 (width) $\times H$ (height). The size of L , W and H was determined after considera-
 150 tion of the sensitivity of numerical results to the domain size; numerical studies
 151 of domain-size dependence are presented in Section 3.3. All computational re-
 152 sults that follow were obtained from numerical solutions of the three-dimensional
 153 governing equations for gas-liquid/liquid-liquid flows. Computations are initial-
 154 ized with a spherical bubble (or drop) of radius $R = 5$ mm set at the center of
 155 the computational domain. The bubble (or drop) is then subjected to a linear
 156 shear flow generated by the motion of the top and bottom plates, which have
 157 constant velocity $+V$ and $-V$, respectively. In the interior of the domain, the
 158 initial velocity condition is assumed to be a simple linear profile and periodic
 159 boundary conditions are imposed along the x and y directions. Mathematically,
 160 the initial and boundary conditions are described as follows:

$$\phi(x, y, z, 0) = \sqrt{(x - \frac{L}{2})^2 + (y - \frac{W}{2})^2 + (z - \frac{H}{2})^2} - R \quad (1)$$

$$\mathbf{u}(x, y, z, 0) = \begin{pmatrix} \frac{2V}{H}(z - \frac{H}{2}) \\ 0 \\ 0 \end{pmatrix}$$

$$\phi(x + L, y, z, t) = \phi(x, y, z, t) \quad \phi(x, y + W, z, t) = \phi(x, y, z, t)$$

$$\mathbf{u}(x, y, H, t) = \begin{pmatrix} V \\ 0 \\ 0 \end{pmatrix} \quad \mathbf{u}(x, y, 0, t) = \begin{pmatrix} -V \\ 0 \\ 0 \end{pmatrix}$$

$$\mathbf{u}(x + L, y, z, t) = \mathbf{u}(x, y, z, t) \quad \mathbf{u}(x, y + W, z, t) = \mathbf{u}(x, y, z, t)$$

161 $\phi(x, y, z, t)$ is a material indicator function which is positive in the “matrix”
 162 fluid and negative in the bubble (or drop) fluid. $\mathbf{u}(x, y, z, t)$ is the velocity.

163 Common dimensionless physical parameters used to describe gas-liquid or
 164 liquid-liquid two-phase flows include the Reynolds (Re), Weber (We) (or Ca (=
 165 We/Re)) and Froude (Fr) numbers. Gas-Liquid and Liquid-Liquid two-phase
 166 flow problems are also determined by the density ratio λ and the viscosity ratio
 167 η . In the present study, in order to clearly isolate the effects of λ and η , and
 168 isolate the balance of the driving wall force with the bubble surface tension

169 force, the effect of gravity is not considered ($g = 0$) so that we ignore the effect
 170 of the Fr number ($= \frac{\Gamma R}{\sqrt{gR}}$).

171 When comparing with previous drop studies, we fix $\lambda = 1$ for the drop cases.
 172 As a result, (for $\lambda = 1$) the following dimensionless physical parameters are used
 173 to describe the problem of drop deformation/breakup in shear flow:

$$Re = \frac{\rho_m U R}{\mu_m}, \quad Ca = \frac{\mu_m U}{\sigma}, \quad \eta = \frac{\mu_b}{\mu_m} \quad m = \text{matrix fluid} \quad (2)$$

174 U is the velocity scale and σ denotes the surface tension. For the problem of
 175 shear-induced drop deformation and breakup, the velocity is set to,

$$U = \Gamma R,$$

176 where the shear-rate is,

$$\Gamma = 2V/H.$$

177 As mentioned in the introduction, most previous drop studies set $\eta = 1$ (e.g. Li
 178 et al. [33]). Thus, for comparison with previous drop deformation and breakup
 179 problems, we set $\lambda = \eta = 1$ (and also neglect the effect of gravity so that
 180 $g = 0$). On the other hand, in our computations for bubble deformation, we
 181 set the density and viscosity of air to be $\rho_b = 1.2 \text{ kg/m}^3$ and $\mu_b = 1.8 \times 10^{-5}$
 182 Pa·s respectively. We emphasize that for consistency with previous studies (Li
 183 et al. [33], Rust and Manga [50], Müller-Fischer et al. [36], Komrakova et al.
 184 [29], Amani et al. [1]), we computationally examine the deformation and breakup
 185 of a bubble in simple linear shear flow as a function of the Re and Ca numbers.
 186 That is to say, by setting $g = 0$, we are isolating the effect of only varying Re and
 187 Ca on bubble deformation and breakup. In our controlled study, we determine
 188 the critical Re_c versus Ca curve in which Re_c corresponds to the threshold of
 189 bubble (or drop) breakup. We determine the critical Re_c versus Ca curve for
 190 strategic pairs of the density ratio and viscosity ratio.

191 In our computations, the density of the matrix fluid is fixed at $\rho_m = 1000$
 192 kg/m^3 . The surface tension at the bubble (drop) interface is $\sigma = 2.5 \times 10^{-2}$
 193 N/m. The values of Re and Ca in our simulations are controlled by changing
 194 the values of μ_m and V . Specifically, we set $\mu_m = 2.0 \times 10^{-2} \sim 6.0 \times 10^{-2}$
 195 Pa·s and $V = \text{about } 1.1 \sim 1.3 \text{ m/s}$. As a consequence, for studying bubble
 196 deformation and break-up, the density and viscosity ratios satisfy $\lambda = 1.2 \times 10^{-3}$
 197 and $\eta < 1.0 \times 10^{-3}$.

198 For readers' reference, we describe the effect of gravity here. When we apply
 199 $g = 9.8 \text{ m/s}^2$, Fr can be $Fr = 1.7 \sim 1.9$ in our computations. Although
 200 the values of Fr are not so large, the effect of gravity (inducing bubble rise
 201 motion) may not be completely negligible in terms of Fr . However, bubbles in
 202 our computations reach the breakup by way of deformation very quickly at t
 203 = about 0.5 s. Accordingly, it is expected that the effect of gravity (inducing
 204 bubble rise motion) can be small for the behavior of bubble deformation and
 205 breakup around critical Re number conditions in our study.

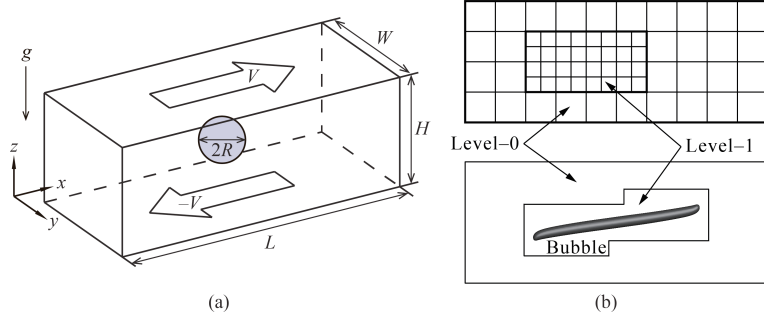


Figure 1: (a) Computational domain schematic for a bubble or drop in shear flow. Gravity is set to zero in our computations in order to isolate the effects of density and viscosity ratios. (b) (upper panel) a two-level adaptive mesh refinement (AMR) grid schematic corresponding to one of our simulations; (lower panel) snapshot of bubble deformation in simple linear shear flow.

206 3. Numerical Analysis

207 3.1. Numerical method and governing equations

208 Numerical results were obtained using the interface capturing Coupled Level
 209 Set and Volume of Fluid (CLSVOF) method (Sussman and Puckett [59], Suss-
 210 man et al. [61]), which is based on a fixed grid finite volume algorithm. The
 211 CLSVOF method is a robust numerical technique that combines some of the ad-
 212 vantages of the Volume of Fluid (VOF) method (Hirt and Nichols [20]) and the
 213 Level Set (LS) (Sussman et al. [60]) method while overcoming their weaknesses.
 214 In the VOF method, the Volume Fraction function, F , is used to represent
 215 the interface. The values of F correspond to the volume fraction of liquid in
 216 a given computational cell. In other words, $F = 0$ when a computational cell
 217 contains only gas and $F = 1$ when a computational cell contains only liquid.
 218 If $0 < F < 1$, then a computational cell contains the gas-liquid interface. The
 219 VOF method has an advantage over the LS method in that accurate algorithms
 220 for advecting F can be applied so that mass/volume is conserved up to machine
 221 precision while still maintaining a sharp representation of the interface. On
 222 the other hand, the disadvantage of the VOF method in comparison to the LS
 223 method is that tangled and difficult reconstruction procedures are required for
 224 determining the slope of the piecewise linear VOF reconstructed interface. In
 225 the LS method, the signed distance function ϕ (LS function) is used to track the
 226 interface. The interface is implicitly represented by the set of points in which
 227 $\phi = 0$. Liquid and gas regions are defined as $\phi > 0$ in the liquid and $\phi < 0$ in the
 228 gas, respectively. One of the advantages of the LS method is that one can track
 229 and represent smoothly the interface, but the LS method has the disadvantage
 230 that mass/volume is not explicitly conserved. In the CLSVOF method, the cou-
 231 pling between the LS function and the VOF function occurs when computing
 232 the normal of the reconstructed interface in the VOF calculation process and
 233 also when assigning the LS function with the exact signed normal distance to
 234 the reconstructed interface in the LS calculation process. That is to say, the

piecewise linear approximation (the volume-of-fluid reconstruction step) for the VOF method is determined using the unit normal vector (\mathbf{n}) estimated from information of the LS function. By taking advantage of both methods, the evolution of the liquid-gas interface location can be computationally captured in such a way so that volume/mass is preserved to machine precision and at the same time, the interface normals and the surface tension force (which is proportional to the interface curvature) can be straightforwardly derived from the smooth level set function.

In our studies, the two-phase fluid flow is comprised of air and a viscous Newtonian liquid. The Heaviside function, $\mathcal{H}(\phi)$, which is defined as

$$\mathcal{H}(\phi) = \begin{cases} 1 & \phi \geq 0 \\ 0 & \phi < 0 \end{cases} \quad (3)$$

will be used below to distinguish each of the two fluids. A single set of three-dimensional equations governs the motion of both fluids, which are taken to be incompressible, and consists of the continuity equation and the Navier-Stokes equations with surface tension forces:

$$\nabla \cdot \mathbf{u} = 0 \quad (4)$$

$$\frac{\partial \mathbf{u}}{\partial t} + (\mathbf{u} \cdot \nabla) \mathbf{u} = \frac{1}{\rho} \nabla \cdot (-p \mathbf{I} + 2\mu \mathbf{D}) + \mathbf{g} - \frac{\sigma\kappa}{\rho} \nabla \mathcal{H} \quad (5)$$

We remark that our method is a “sharp interface method[61, 57, 27]. Thereby we do not need to specify an empirical interface thickness parameter[60, 59].

\mathbf{u} is the velocity vector, t represents time, p is the pressure, \mathbf{I} is the unit tensor, \mathbf{D} is the rate of deformation tensor ($\mathbf{D} = \frac{1}{2}(\nabla \mathbf{u} + (\nabla \mathbf{u})^T)$), ρ is the density, μ is the viscosity, κ is the interfacial curvature, and the Heaviside function $\mathcal{H}(\phi)$ is a function of the level set (LS) function ϕ . The singular Heaviside gradient term in the right hand side of equation (5) is a body force representing the surface tension force and is equivalent to specifying that the jump in the normal stress is equal to $\sigma\kappa$ (Tanguy et al. [62]). The surface tension force expressed by the singular Heaviside gradient term acts only on the gas-liquid interface. The sharp interface “Ghost Fluid Method” (Kang et al. [27]) is used to discretize the gradient of the Heaviside function as it appears in the surface tension force term. This force, upon discretization, is only non-zero across cells in which the level set function changes sign.

The interfacial curvature κ is computed with second order accuracy directly from the volume-of-fluid (VOF) function and the level set function using the height function technique (Sussman [57], Sussman et al. [61]). We remark that we get the same results if we were to compute κ directly from the LS function using the “level set” height function technique.

Since ρ and μ are taken to be constant in each fluid, with a jump at the interface, they can be expressed in terms of the Heaviside function,

$$\rho = \rho_m \mathcal{H} + \rho_b (1 - \mathcal{H}), \quad \mu = \mu_m \mathcal{H} + \mu_b (1 - \mathcal{H}). \quad (6)$$

²⁷⁰ The subscripts “b” and “m” refer to “drop or bubble” and “matrix fluid”,
²⁷¹ respectively. To represent the free surface with the CLSVOF method, we must
²⁷² evolve the solution to both the VOF equation for F and the LS equation for ϕ :

$$\frac{\partial F}{\partial t} + (\mathbf{u} \cdot \nabla) F = 0, \quad \frac{\partial \phi}{\partial t} + (\mathbf{u} \cdot \nabla) \phi = 0. \quad (7)$$

²⁷³ In all computations, the discretized variables p , ϕ and F are located at the
²⁷⁴ cell centers and the discrete velocity variable \mathbf{u} is located at cell face centers.
²⁷⁵ Our computations are performed using an overall second-order accurate hydro-
²⁷⁶ dynamic scheme. The spatial discretization uses second-order accurate, slope-
²⁷⁷ limited, upwind techniques for the nonlinear advective terms. The velocity and
²⁷⁸ pressure fields are computed using an implicit pressure projection procedure.

²⁷⁹ The temporal discretization of our numerical method is an operator split
²⁸⁰ projection method as described by Sussman et al. [61]. An outline of our method
²⁸¹ is as follows (see Sussman et al. [61], section 4, for more details):

All Steps. Timestep

²⁸² The timestep, Δt , is governed by the CFL condition and surface tension
²⁸³ (section 5.7 of Sussman et al. [61]):

$$\Delta t < \min_{i,j,k} \left(\frac{\Delta x}{2|U^n|}, \frac{1}{2} \sqrt{\frac{\rho^L}{8\pi\sigma}} \Delta x^{3/2} \right)$$

Step 1. CLSVOF interface advection

$$\begin{aligned} \phi^{n+1} &= \phi^n - \Delta t [\mathbf{u} \cdot \nabla \phi]^n \\ F^{n+1} &= F^n - \Delta t [\mathbf{u} \cdot \nabla F]^n \end{aligned}$$

Step 2. Nonlinear advective force terms

$$\mathcal{A} = [\mathbf{u} \cdot \nabla \mathbf{u}]^n$$

Step 3. Viscosity force

$$\frac{\mathbf{u}^* - \mathbf{u}^n}{\Delta t} = -\mathcal{A} + g\vec{z} - [\nabla p / \rho]^n + \frac{1}{2} \frac{\nabla \cdot (2\mu \mathbf{D}^n) + \nabla \cdot (2\mu \mathbf{D}^*)}{\rho}$$

²⁸⁴ Step 4. Pressure projection and ghost fluid surface tension algorithm

$$\mathbf{V} = \mathbf{u}^n + \Delta t (-\mathcal{A} + g\vec{z} + \frac{1}{2} \frac{\nabla \cdot (2\mu \mathbf{D}^n) + \nabla \cdot (2\mu \mathbf{D}^*)}{\rho})$$

²⁸⁵

$$\mathbf{V} = \mathbf{V} - \Delta t \frac{\sigma \kappa(\phi^{n+1})}{\rho} \nabla \mathcal{H}(\phi^{n+1})$$

286

$$\nabla \cdot \frac{\nabla p}{\rho} = \frac{1}{\Delta t} \nabla \cdot \mathbf{V}$$

287

$$\mathbf{u}^{n+1} = \mathbf{V} - \Delta t \frac{\nabla p}{\rho}$$

288 To make efficient use of computational resources, our numerical simulations
 289 utilize an adaptive hierarchy of grids based on a dynamic adaptive mesh refine-
 290 ment (AMR) technique (Sussman et al. [58]). Adaptive grids are dynamically
 291 adjusted based on the location of the deforming gas-liquid interface. In the
 292 AMR technique, the grid resolution is increased in regions near the interface
 293 while a coarser grid is used where the flow is relatively steady. The upper panel
 294 of Figure 1(b) displays a schematic view of the hierarchical grid structure and
 295 the lower panel corresponds to an actual computational example corresponding
 296 to bubble deformation in simple linear shear flow. In general, the mesh hier-
 297 archy is composed of different levels of refinement ranging from coarsest $\ell = 0$
 298 (“level-0”) to finest $\ell = \ell_{\max}$ (“level- ℓ_{\max} ”). The refinement ratio of one grid
 299 size ($\Delta x = \Delta y = \Delta z$) to the next finer level is two so that $\Delta x^{\ell+1} = 0.5\Delta x^\ell$. All
 300 computations in this study used an AMR system with a maximum prescribed
 301 level $\ell_{\max} = 1$ (as illustrated in the upper panel of Figure 1(b)). In our adaptive
 302 mesh refinement algorithm, the velocity in the coarse grid cells that neighbor
 303 fine grid cells is interpolated from the coarse grid using bilinear interpolation in
 304 order to initialize “ghost” fine cells. Thus, the bilinear interpolation procedure
 305 produces interpolated fine grid data as a linear combination of the coarse grid
 306 data.

307 Remark 1: Due to time step stability constraints, the variable density pres-
 308 sure projection process, and computed bubble shapes with high aspect ratio,
 309 we find that our simulations can take over six months. We have experimented
 310 with (a) decreasing the “error buffer” parameter (radius of cells to be tagged
 311 when a given cell is tagged for adaptivity) and (b) relaxing the condition that
 312 the bubble-liquid interface be wholly contained on the finest adaptive level.
 313 Unfortunately we have found that these steps lead to poorer accuracy. This
 314 “diminishing returns” phenomena is expected for low Mach number flows in
 315 which the incompressible flow equations are characterized by non-local behav-
 316 ior. We refer the reader to the following research[34] in which it has been found
 317 through a systematic study that using an AMR grid can be less accurate than
 318 a case with a uniform fine grid (luckily that is not the case here). To summa-
 319 rize: we have found that each further refinement of the grid will multiply the
 320 simulation time by a factor of about eight (factor of 4 due to spatial refinement,
 321 factor of 2 due to temporal refinement).

322 Remark 2: We believe that the inclusion of a special sub-scale model right
 323 at the point of bubble break-up is unnecessary because the driving shear force
 324 is temporally uniformly applied instead of impulsively applied. We are aware of
 325 research for predicting whether droplets merge or bounce[32] but this research

326 is not applicable in our case. We are not aware of previous studies on the shear
 327 flow driven breakup of bubble or drops that implement special subscale models.
 328

329 *3.2. Validation of the numerical method*

330 The effectiveness of our sharp interface computational method has been
 331 demonstrated via grid refinement studies and comparison with experiments for
 332 the complicated rising motion of single bubbles and drops in viscous liquids
 333 Ohta and Sussman [41], Ohta et al. [37, 38, 42], Stewart et al. [55], Sussman
 334 et al. [61], the simulation of atomization in a realistic diesel injector[2], and the
 335 simulation of bubble formation due to the injection of gas through a nozzle[40].
 336 In this section, the accuracy of our computational method will be verified for
 337 the problem of shear-induced deformation of a drop and bubble. First, we com-
 338 pare quantitatively against the steady-state drop deformation results reported
 339 by Li et al. [33]. The shape of a deformed drop in simple linear shear flow is de-
 340 scribed in terms of the Taylor deformation parameter $D=(a-b)/(a+b)$, where
 341 a and b are the major and minor axes of the deformed drop respectively. For
 342 consistency, we perform numerical simulations using CLSVOF over the same
 343 computational domain and grid size used in Li et al. [33], which has dimensions
 344 $L(8R) \times W(4R) \times H(8R)$ (recall that R is the bubble/drop radius) and a level-0
 345 grid size $\Delta x = \Delta y = \Delta z = R/8$; our two-level AMR grid structure also uses a
 346 finer level-1 grid size $\Delta x^{\ell=1} = \Delta y^{\ell=1} = \Delta z^{\ell=1} = R/16$. Numerical results are
 347 listed in Table 1 for D as a function of Re , with $Ca = 0.3$ and $\lambda = \eta = 1$ fixed
 348 in every case. The results in Table 1 compare computations using our CLSVOF
 349 algorithm with corresponding results that were obtained with the VOF method
 used in Li et al. [33].

Table 1: Comparison of the Taylor deformation parameter D for a drop as a function of Re ($Ca = 0.3$, $\lambda = \eta = 1$). In all cases, the domain size is $L(8R) \times W(4R) \times H(8R)$, where R is the drop radius. The CLSVOF method computations used a two-level AMR computational domain with a level-0 discretization $\Delta x^{\ell=0} = \Delta y^{\ell=0} = \Delta z^{\ell=0} = R/8$ and a level-1 discretization $\Delta x^{\ell=1} = \Delta y^{\ell=1} = \Delta z^{\ell=1} = R/16$.

Reynolds number	0.1	0.5	0.6	0.75
D (Li et al. [33])	0.3968	0.45	0.4768	Breakup
D (Our study)	0.3960	0.4570	0.4758	Breakup

350 Next, we examine the validation of our computational method in which
 351 we compare with the “bubble deformation in simple linear shear flow” results
 352 reported by Müller-Fischer et al. [36]. Müller-Fischer et al. [36] experimentally
 353 inquired into the bubble deformation under the condition of $Re \approx 0$. In our
 354 study, we computed the bubble deformation on a computational domain with
 355 dimensions $L(12R) \times W(6R) \times H(6R)$ and a computational grid in which the
 356 finest level grid size was $\Delta x^{\ell=1} = \Delta y^{\ell=1} = \Delta z^{\ell=1} = R/16$. Computations
 357 were performed for the conditions of $Ca = 0.96$ and $Ca = 1.63$ with $Re \approx 0$
 358 ($Re = 5.0 \times 10^{-4}$), $\lambda = 1.2 \times 10^{-3}$ and $\eta \leq 1.2 \times 10^{-6}$. The prescribed parameters
 359

360 are consistent with the experimental conditions by Müller-Fischer et al. [36].
 361 Comparisons of our numerical results and previous experimental results (Müller-
 362 Fischer et al. [36]) are tabulated in Table 2. Additionally, in Table 2, we also list
 363 experimental results with the condition of $Re \approx 0$ and $\lambda \approx \eta \approx 0$ by Rust and
 364 Manga [50]. These experimental values were obtained from the graph showing
 365 the relation of D vs Re (Rust and Manga [50]). As is clear from Table 2, our
 366 numerical results predicted larger values of D than experimental ones reported
 367 by Müller-Fischer et al. [36]. Nevertheless, our numerical results are very close to
 368 the experimental results by Rust and Manga [50], which emphasizes the intrinsic
 369 difficulties associated with experimental investigations of bubble dynamics, even
 370 in simple linear shear flow. These comparisons suggest that our computational
 371 method is effective and robust at reproducing bubble dynamics in simple linear
 shear flow.

Table 2: Comparison of D for a bubble as a function of Ca ($Re \approx 0$, $\lambda \approx \eta \approx 0$). In all cases, the domain size is $L(12R) \times W(6R) \times H(6R)$. The CLSVOF computations used a two-level AMR computational domain with a level-0 discretization $\Delta x^{\ell=0} = \Delta y^{\ell=0} = \Delta z^{\ell=0} = R/8$ and a level-1 discretization $\Delta x^{\ell=1} = \Delta y^{\ell=1} = \Delta z^{\ell=1} = R/16$.

Capillary number	0.96	1.63
D (Müller-Fischer et al. [36])	0.37	0.58
D (Rust and Manga [50])	0.71 ± 0.05	0.81 ± 0.02
D (Our study $\Delta x^{\ell=1} = R/16$)	0.63	0.71

372
 373 Finally, we present a comparison with numerical results for drop breakup
 374 reported in Renardy and Cristini [49]. Figure 2 demonstrates drop breakup with
 375 pinch-off behavior for three Re and Ca conditions and with constant values of
 376 $\lambda = \eta = 1$ for all cases. The three cases that we consider correspond to (a)
 377 $Re = 10$, $Ca = 0.16$, (b) $Re = 12$, $Ca = 0.1753$, and (c) $Re = 15$, $Ca =$
 378 0.196, and which are illustrated in Figures 2(a)-(c), respectively. The results
 379 reported in Renardy and Cristini [49], which were obtained with a VOF method,
 380 are shown inside boxes while results obtained with our CLSVOF approach are
 381 displayed outside boxes. In the computations presented in Renardy and Cristini
 382 [49], the dimensions $W = 4R$ and $H = 8R$ were fixed, while L was changed
 383 depending on Re and Ca conditions, and the grid size was set to $\Delta x = \Delta y =$
 384 $\Delta z = R/8$. To compare with their results, we performed simulations with the
 385 CLSVOF method over a two-level AMR computational domain of the same
 386 dimensions and the same level-0 discretization: $\Delta x^{\ell=0} = \Delta y^{\ell=0} = \Delta z^{\ell=0} =$
 387 $R/8$; we set the finer level-1 grid size $\Delta x^{\ell=1} = \Delta y^{\ell=1} = \Delta z^{\ell=1} = R/16$. The
 388 results shown in Figure 2 verify that our numerical approach can reproduce
 389 the same drop breakup behavior presented in Renardy and Cristini [49]. Slight
 390 differences between the results can be attributed to the increased resolution used
 391 in our study in the level-1 grid around the elongated drop.

392 The numerical validation studies performed in this section and the follow-
 393 ing section demonstrate that our numerical method can reliably determine the
 394 transition regions at which shear-induced bubble or drop deformation leads to

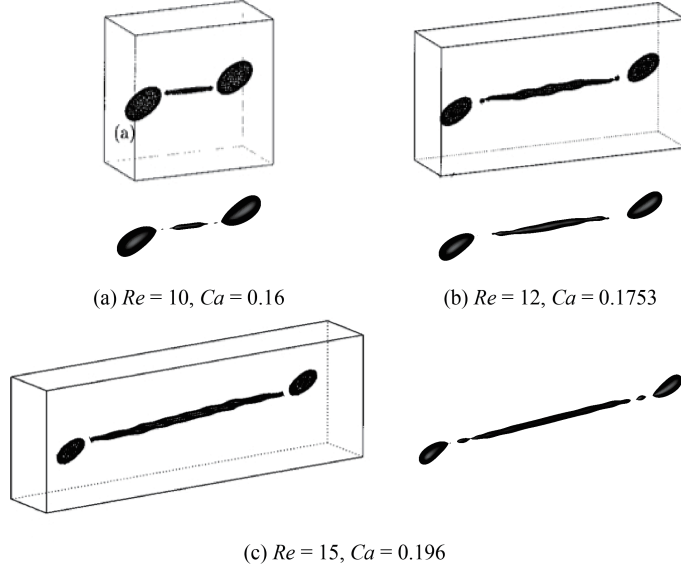


Figure 2: Comparison with results reported in Renardy and Cristini [49] (shown in bounding boxes) for drop breakup in shear flow. In Renardy and Cristini [49], the computational domain dimensions were $W = 4R$, $H = 8R$, and L was varied depending on the Re and Ca conditions. The grid size in Renardy and Cristini [49] was set to $\Delta x = \Delta y = \Delta z = R/8$. Reprinted with permission from reference Renardy and Cristini [49]. Copyright 2001, AIP Publishing. The results obtained with our CLSVOF algorithm, corresponding to each case in reference Renardy and Cristini [49], are shown without the bounding boxes. The CLSVOF method used a two-level AMR computational domain with a level-0 discretization $\Delta x^{\ell=0} = \Delta y^{\ell=0} = \Delta z^{\ell=0} = R/8$ and a level-1 discretization $\Delta x^{\ell=1} = \Delta y^{\ell=1} = \Delta z^{\ell=1} = R/16$. The onset of drop breakup is demonstrated for (a) $Re = 10$, $Ca = 0.16$, (b) $Re = 12$, $Ca = 0.1753$, and (c) $Re = 15$, $Ca = 0.196$. For all three Re and Ca conditions, $\lambda = \eta = 1$.

breakup. We remark that in the next section, we demonstrate that we can expect an error of 3% for predicting the transition to break-up. The analysis in this section and the following also demonstrate that the error is reduced by a factor of 2 each time the grid is refined by a factor of 2. We reiterate that we have found at least a factor of 2 error reduction for each grid refinement in a number of multiphase flow problems involving complex interface deformation and breakup; see Ohta and Sussman [41], Ohta et al. [37, 38, 42], Stewart et al. [55], Sussman et al. [61], Arienti et al. [2], Ohta et al. [40].

3.3. Consideration of domain and grid sizes

3.3.1. Selecting the appropriate domain size

The computational domain size used in numerical studies can affect the behavior of drop deformation and breakup. Referring to Figure 1(a), with an appropriately large domain length L and a fixed width $W = 4R$, the effect of the height H on drop behavior was examined in Li et al. [33] for Stokes flows and various Ca conditions and in Komrakova et al. [29] for $Re = 1$ and $Ca =$

⁴¹⁰ 0.27. Other related studies investigated drop breakup sensitivity (Renardy and
⁴¹¹ Cristini [47]) and drop deformation sensitivity (Renardy et al. [48]) with respect
 to the entire domain size.

Table 3: Comparison of the Taylor deformation parameter D for a drop as a function of domain size ($Re = 0.75$, $Ca = 0.3$, $\lambda = \eta = 1$). CLSVOF method computations used a two-level AMR computational domain with a level-0 discretization $\Delta x^{\ell=0} = \Delta y^{\ell=0} = \Delta z^{\ell=0} = R/8$ and a level-1 discretization $\Delta x^{\ell=1} = \Delta y^{\ell=1} = \Delta z^{\ell=1} = R/16$.

System	Domain size ($L \times W \times H$)	D
System 1	$8R \times 4R \times 8R$	Breakup
System 2	$12R \times 4R \times 8R$	Breakup
System 3	$8R \times 4R \times 6R$	0.541
System 4	$8R \times 6R \times 6R$	0.466
System 5	$8R \times 8R \times 8R$	0.460
System 6	$8R \times 16R \times 16R$	0.460

⁴¹²
⁴¹³ Here we investigate the drop dynamics sensitivity to domain size around
⁴¹⁴ the critical Reynolds number $Re_c = 0.75$. Specifically, we consider domain size
⁴¹⁵ sensitivity for the condition of $Re = 0.75$, $Ca = 0.3$, and $\lambda = \eta = 1$, which is a
⁴¹⁶ condition used in the comparison studies of the previous section. As shown in
⁴¹⁷ Table 1, the drop breaks up for the condition of $Re = 0.75$ and $Ca = 0.3$ with
⁴¹⁸ a domain size of $L(8R) \times W(4R) \times H(8R)$. Results for domain size sensitivity
⁴¹⁹ for six domain systems, all of which use a level-1 grid size $\Delta x^{\ell=1} = \Delta y^{\ell=1} =$
⁴²⁰ $\Delta z^{\ell=1} = R/16$, are tabulated in Table 3. Note that the domain size used in the
⁴²¹ comparison study (Table 1) corresponds to System 1.
⁴²²

⁴²³ The results in Table 3 suggest that drop deformation is promoted when we
⁴²⁴ use a domain size with $W = 4R$. In contrast, the drop does not break up and
⁴²⁵ becomes stable with a deformed shape if we set L large enough and $W \geq 6R$ and
⁴²⁶ $H \geq 6R$. Since the value of D for the domain size $L(8R) \times W(6R) \times H(6R)$ differs
⁴²⁷ by only 1.3% with the value for the domain size of $L(8R) \times W(16R) \times H(16R)$,
⁴²⁸ in the results that follow we set the width to $W = 6R$ and the height to $H = 6R$
⁴²⁹ to minimize the number of computational grid nodes along those directions. To
⁴³⁰ determine the critical Reynolds number Re_c (with $Ca = 0.3$), we consider a
⁴³¹ domain size of $L(24R) \times W(6R) \times H(6R)$, and we find that the drop reaches a
⁴³² stable state with deformation parameter $D=0.549$ for $Re = 1.0$, while a value
⁴³³ of $Re = 1.1$ leads to drop breakup.

⁴³³ 3.3.2. Selecting the appropriate grid size

⁴³⁴ The grid size and adaptive meshing strategy that we adopt is chosen in order
⁴³⁵ to answer the research question as to the conditions which determine whether
⁴³⁶ a bubble in shear flow will break-up or not. In such a case, we must accurately
⁴³⁷ capture the balance of forces with respect to the (non-local) force exerted from
⁴³⁸ the wall driven flow acting against the interfacial surface tension force. The
⁴³⁹ accuracy of the “Critical Reynolds Number” depends on the largest Taylor De-
⁴⁴⁰formation parameter D that is supported by the grid (see e.g. Figures 8 and

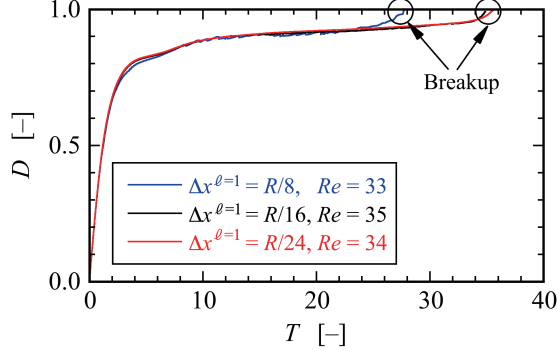


Figure 3: Time evolution of the deformation parameter D versus dimensionless time $T = \Gamma t$ for a bubble, obtained with three grid systems at different resolutions. All three resolutions use a two-level AMR grid with an effective fine resolution grid size $\Delta x^{\ell=1} = \Delta y^{\ell=1} = \Delta z^{\ell=1}$. The evolution of D using the first system, where $\Delta x^{\ell=1} = R/8$, is shown in blue and it predicts that bubble breakup occurs at a Reynolds number $Re = 33$. The evolution of D using the second system, where $\Delta x^{\ell=1} = R/16$, is shown in black and it predicts that bubble breakup occurs at a Reynolds number $Re = 35$. Results with the third system, shown in red, use $\Delta x^{\ell=1} = R/24$, and they predict that breakup occurs at $Re = 34$. The capillary number corresponding to these results is $Ca = 1.0$. ($\lambda = 1.2 \times 10^{-3}$, $\eta < 1.0 \times 10^{-3}$)

11). As we report here, we have found that as long as the grid size is fine enough
 441 to support a Taylor Deformation parameter $D < 0.95$, then the transition re-
 442 gion (i.e. “Critical Reynolds number”) (see Figures 3 and 12) will be captured
 443 with a tolerance of three percent. The simulation time becomes impractical if
 444 we were to try to further improve the “critical Reynolds number” accuracy. A
 445 smaller tolerance would necessitate a larger supported Deformation parameter
 446 D which would in turn necessitate a higher aspect ratio computational domain,
 447 increased droplet surface area at break-up, increased number of time steps, and
 448 higher resolution for representing the drop/bubble at its thinnest point.

449 We make the distinction between our present research, and the research
 450 found in the work of Zhang et al. [73, 74] on predicting the conditions for bubble
 451 mergers. Even in the most extreme cases for mergers, the largest Deformation
 452 parameter never exceeds 0.4 in Zhang et al. [73]. In summary, our gridding
 453 requirements necessitate grid points distributed relatively evenly throughout the
 454 computational domain when a bubble is stretched to a $D = 0.9$ Deformation,
 455 whereas in Zhang et al. [73] the gridding strategy necessitates a more localized
 456 strategy.

457 The numerical results presented in this and the previous section used a
 458 finest-level grid size set to $\Delta x^{\ell=1} (= \Delta y^{\ell=1} = \Delta z^{\ell=1}) = R/16$. To verify the
 459 adequacy of this grid resolution, we present grid refinement results for a bubble
 460 breakup simulation with $Ca = 1.0$, which corresponds to the most deformable
 461 and stretchable bubble case considered in our numerical studies. We use three
 462 different grid systems, (i) $\Delta x^{\ell=1} = R/8$, (ii) $\Delta x^{\ell=1} = R/16$, and (iii) $\Delta x^{\ell=1} =$
 463 $R/24$, in order to determine Re_c . Figure 3 shows the time evolution of the

465 deformation parameter D over time for the three grid systems; the x -axis is a
 466 dimensionless time defined by $T = \Gamma t$ and the y -axis is D . The results show that
 467 bubble breakup occurs at $Re_c = 35$ for the grid system with $\Delta x^{\ell=1} = R/16$,
 468 while the finer computational grid with $\Delta x^{\ell=1} = R/24$ predicts a critical value of
 469 $Re_c = 34$. For the $\Delta x^{\ell=1} = R/8$ results, it is clear that the $R/8$ resolution is too
 470 coarse in order to capture the proper break-up time, albeit the critical Reynolds'
 471 number, $Re_c = 33$, was still close to the finer grid resolution cases. Note that
 472 although the time evolution of D for the two finer resolution systems ($R/16$ and
 473 $R/24$) is consistent between the two, (the predicted critical Reynolds numbers
 474 differ by $\sim 3\%$), the computational time using the grid system with $\Delta x^{\ell=1} =$
 475 $R/24$ was more than 6 times longer than the one based on the coarser system
 476 with $\Delta x^{\ell=1} = R/16$. We remark that in our search for Re_c , we considered a wide
 477 range of values of Ca and we found it necessary to use a large L ($\sim 24R$) since
 478 for certain shear flows the bubble can stretch significantly without breaking up.
 479 Nevertheless, for the conditions presented in this section, the results indicate
 480 that our numerical approach, even with a finest-level resolution set to $\Delta x^{\ell=1} =$
 481 $R/16$, is capable of accurately reproducing bubble deformation and breakup
 482 without sacrificing any essential dynamical features.

483 **4. Results and Discussion**

484 *4.1. Drop deformation and breakup*

485 To illustrate the differences in deformation and breakup between a drop
 486 and a bubble around critical conditions, we first present numerical results for
 487 drop deformation. The time evolution of drop deformation and breakup in
 488 simple linear shear flow for two conditions is shown in Figure 4; the first case,
 489 shown in Figure 4(a), uses $Ca = 0.3$ and $Re = 1.0$, while the second case,
 490 depicted in Figure 4(b), uses $Ca = 0.3$ and $Re = 1.1$. Using a domain size of
 491 $L(24R) \times W(6R) \times H(6R)$, in the case with $Re = 1.0$, the drop gradually deforms
 492 and finally attains a stable deformed state. **After $T = 35.0$, the drop remains a**
 493 **stable deformed state with $D = 0.549$.** Over the same domain, for the case with
 494 $Re = 1.1$, the “mother” drop elongates over time and the volume at the ends
 495 of the deforming drop expands; that is, both ends of the drop become bulb-
 496 shaped. As time progresses, particularly over the time interval $48.4 \leq T \leq 55.2$,
 497 a thread-bridge forms between the bulbous ends and the thread-bridge becomes
 498 thinner. Finally, at around the dimensionless time $T \sim 56.7$, the mother drop
 499 breaks up, forming two “daughter” drops through the pinch off; one satellite
 500 drop is also generated between the pinched off daughter drops.

501 *4.2. Bubble deformation and breakup*

502 Next we present numerical results that illustrate the conditions that lead
 503 to bubble deformation without breakup as well as conditions where the bubble
 504 deforms and ultimately breaks up. The time evolution of shear-induced bubble
 505 deformation without breakup at the condition of $Ca = 0.3$ and $Re = 92$ is
 506 depicted in Figure 5 and the bubble breakup process with flow condition of

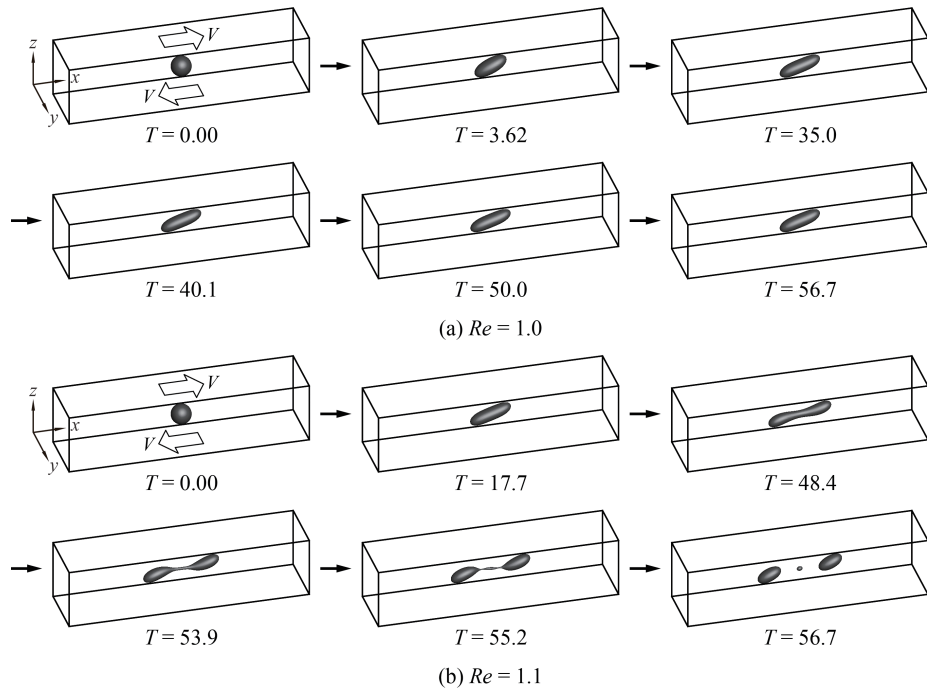


Figure 4: Time evolution of drop deformation and breakup in shear flow at the condition of $Ca = 0.3$ with (a) $Re = 1.0$ and (b) $Re = 1.1$. The “drop” critical Reynolds number corresponding to $Ca = 0.3$ is $1.0 < Re_c < 1.1$. ($\lambda = \eta = 1.0$)

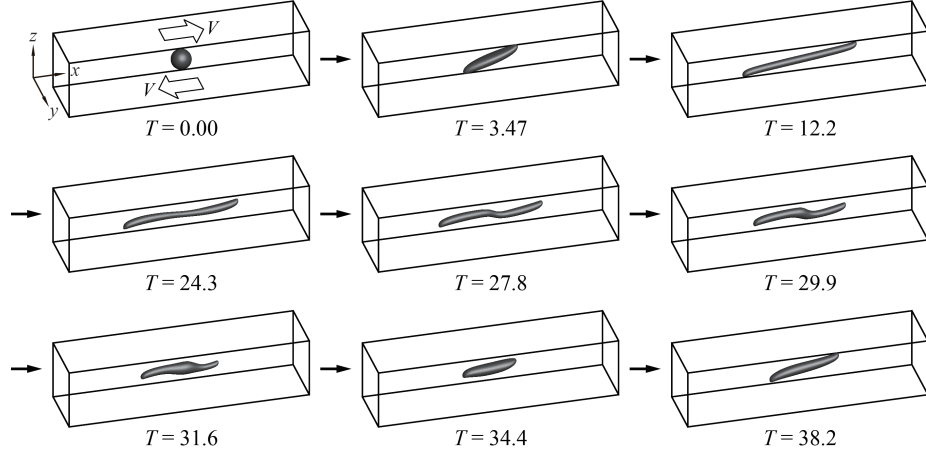


Figure 5: Time evolution of bubble deformation in shear flow at the condition of $Ca = 0.3$ and $Re = 92$. The “bubble” critical Reynolds number corresponding to $Ca = 0.3$ is $92 < Re_c < 93$. In contrast to the drop deformation case, when Re is slightly below Re_c (See Figure 4.1 $Re = 1.0$ for the drop case), the bubble shape will not reach a steady shape, instead the bubble shape alternates between the shapes “slightly stretched” ($T = 3.47$), fully stretched and “doglegged” ($T = 27.8$) and “almost” back to the original “slightly stretched” case ($T = 34.4$). ($\lambda = 1.2 \times 10^{-3}$, $\eta < 1.0 \times 10^{-3}$)

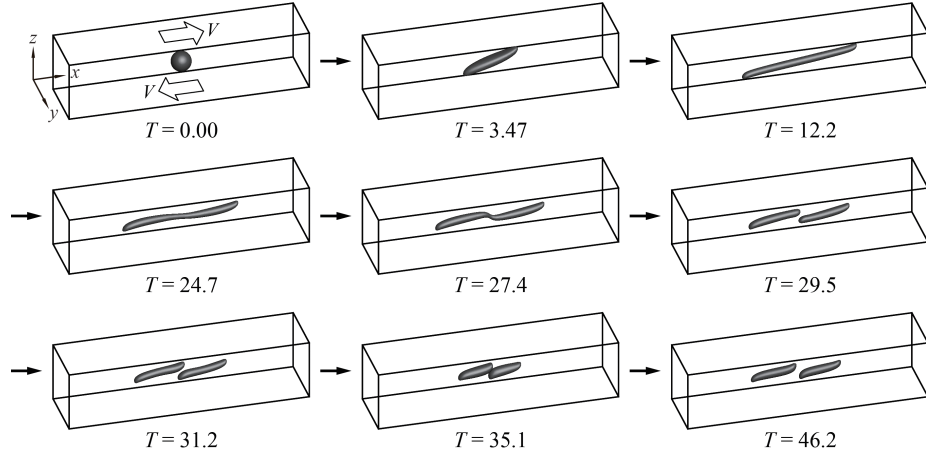


Figure 6: Time evolution of bubble deformation in shear flow at the condition of $Ca = 0.3$ and $Re = 93$. The “bubble” critical Reynolds number corresponding to $Ca = 0.3$ is $92 < Re_c < 93$. ($\lambda = 1.2 \times 10^{-3}$, $\eta < 1.0 \times 10^{-3}$)

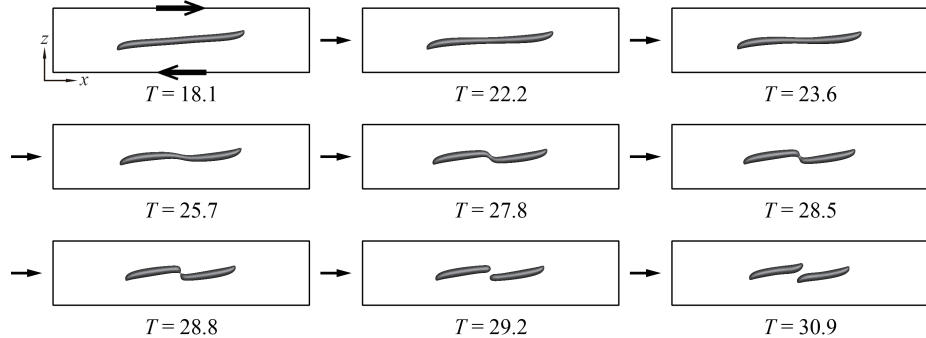


Figure 7: Detail of bubble breakup process in shear flow at the condition of $Ca = 0.3$ and $Re = 93$. The “bubble” critical Reynolds number corresponding to $Ca = 0.3$ is $92 < Re_c < 93$. ($\lambda = 1.2 \times 10^{-3}$, $\eta < 1.0 \times 10^{-3}$)

507 $Ca = 0.3$ and $Re = 93$ is illustrated in Figure 6. The results indicate that
508 the critical Reynolds number is approximately $Re_c = 93$ (with $Ca = 0.3$).
509 A comparison with the drop breakup dynamics presented in Section 4.1 and
510 the corresponding processes for bubble deformation and breakup exhibit very
511 distinct features. First, we note that a relatively large shear force magnitude is
512 required for bubble breakup ($\lambda = 1.2 \times 10^{-3}$, $\eta < 1.0 \times 10^{-3}$) compared with the
513 case of the drop ($\lambda = \eta = 1$). Then, for the same value of $Ca = 0.3$, the critical
514 Reynolds number for the bubble is around 85 times larger than that for the
515 drop. Focusing on the bubble dynamics with no-breakup (Figure 5), the results
516 show that the bubble is largely elongated in the x -direction at the early stages
517 ($T \leq 24.3$) of bubble deformation, but the bubble does not develop the bulb-
518 like shape (large volume areas) at both ends present in the drop deformation
519 process. It is also evident that the ends of the deforming bubble develop cusped
520 shapes under the influence of the strong shear flow. In providing a more detailed
521 description, very large shear forces are required to deform the bubble because
522 $\lambda \simeq 0$ and $\eta \simeq 0$. Thus, the bubble undergoing large shear forces at $T > 0$
523 is largely stretched long the shear flow direction, and the very long elongated
524 bubble with cusped shapes is formed. Accordingly, the bubble finally breaks up
525 through f the elongated shape without forming a bulb-like shape. A noteworthy
526 feature for the non-breaking bubble is that it does not settle into a deformed
527 stable state as in the case of drop deformation presented in Figure 4.1(a). After
528 an initial elongation process, the bubble enters a shrinking phase ($T = 27.8$)
529 where the doglegged shape formed at the center of the bubble returns to a
530 smaller deformed shape ($T = 34.4$) that is similar to its earlier shape ($T = 3.47$).
531 However, when we compare the early deformed bubble shape at $T = 3.47$ with
532 the shape at $T = 34.4$, it is clear that the shapes are not identical. Following the
533 shrinking phase, the bubble begins to stretch again ($T = 38.2$) and the bubble
534 oscillates between its elongated shape and shortened geometry.

535 For the case of bubble breakup (Figure 6), we observe that the deformation
536 process is almost the same as the no-breakup case until the doglegged shape

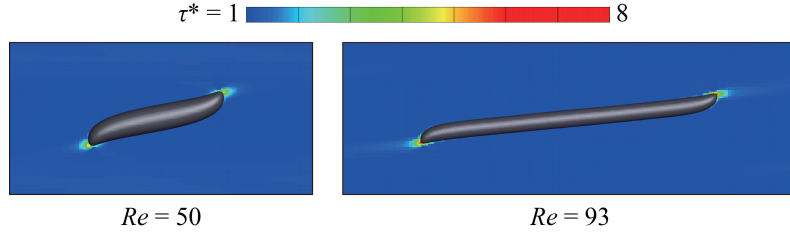


Figure 8: Normalized shear stress τ^* around a bubble for two Reynolds numbers under the condition of $Ca = 0.3$. The left image shows the shear stress profile at $Re = 50$ and the right image at $Re = 93$.

is formed at $T \sim 27.4$. The bubble finally breaks during the time interval $27.7 \leq T \leq 29.5$. For a closer examination of the bubble breakup process, a detailed panel of cross-sectional slices in the xz -plane through the bubble shape center is presented in Figure 7. The images displayed in Figure 7, which are taken at shorter time intervals than those shown in Fig. 6, reveal that the bubble breaks up into two daughter bubbles due to the pinch off at the thread-bridge part of the doglegged shape during the shrinking process ($T = 28.5 \sim 28.8$). After breaking up, the two daughter bubbles migrate to the center: the left daughter bubble moves toward the right-side of the domain and the right daughter bubble moves to the left side (see results for $T = 29.5 \sim 35.1$ in Figure 6 and for $T = 28.8 \sim 30.9$ in Figure 7). The two daughter bubbles then momentarily congregate near the domain center ($T = 35.1$ in Figure 6), before they slowly start to separate: the left daughter bubble moves to the left and the right daughter bubble moves to the right ($T = 46.2$ in Figure 6). The results clearly demonstrate that the bubble breakup process is markedly different from the analogous drop breakup process with $\lambda = 1$ and $\eta = 1$. Note that the appearance of deformation and breakup of the drop will largely depend on the viscosity ratios.

4.3. Shear stress acting on the bubble

In the previous section, the appearance of bubble deformation and breakup was discussed. It is expected that a large deformation and breakup of the bubble are closely related to the state of shear stress acting on the bubble. Figure 8 shows the shear stress profile around a bubble for two Reynolds numbers under the condition of $Ca = 0.3$: Reynolds number equal to 50 and 93. The shear stress profile on the left corresponds to the case of $Re = 50$ and the right side shows the shear stress profile for the case of $Re = 93$. The normalized shear stress, $\tau^* = \tau/\tau_0$, is defined as a ratio of the local shear stress $\tau = \mu_m \sqrt{2\mathbf{D} : \mathbf{D}}$ and the apparent shear stress $\tau_0 = \mu_m \Gamma$. In this study, for a given Ca condition, the same value of τ_0 is used regardless of Re . For the case of $Re = 50$, the bubble reached a deformed stable state, and the shear stress profile around the bubble was drawn after the bubble attained a stable deformed state. As observed in previous sections, when the value of Re is slightly below the critical Re

569 condition, the bubble does not settle into a deformed stable state but instead
570 alternates in an elongation and contraction process. **The shear stress profile for**
571 **the case of $Re = 93$ was depicted when the bubble sufficiently elongated ($T =$**
572 **14.9).** In comparison to the $Re = 50$ case on the left, the right image in Fig. 8
573 ($Re = 93$) shows a higher shear stress profile near the bubble endpoints as it
574 undergoes an elongation state in the process toward breakup. The value of the
575 maximum shear stress for the case of $Re = 50$ is $\tau^* \approx 6$ and the maximum shear
576 stress for the case of $Re = 93$ at the moment shown in Fig. 8 has the value of
577 $\tau^* \approx 8$. The shear stress profile in Fig. 8 (color contour) is drawn in the range
578 from $\tau^* = 1$ to $\tau^* = 8$, but, for emphasis, shear stress regions with $\tau^* \geq 6$ are
579 illustrated in red. As can be seen in the figure, the strongest shear stresses are
580 concentrated on the ends of the bubble for both Re conditions. This indicates
581 that the strong shear stresses acting on the ends of the bubble are responsible
582 for much of the bubble stretching. It is important to note that the magnitude
583 of the shear stress acting on the ends of the bubble for the case of $Re = 93$ is
584 much larger than that for the case of $Re = 50$.

585 We also observe that the shear stress inside the bubble was very small relative
586 to that of the matrix fluid due to very small density and viscosity of the bubble.
587 Since the force of strong shear stresses acting on the ends of the bubble is
588 difficult to transfer across the interface, as a consequence, a sufficiently large Re
589 condition is required for large bubble deformations.

590 In summary, what we discover is that for the Reynolds number sufficiently below
591 the critical value, a relatively quick unsteady elongation period gives way to a
592 steady state (with no break up). On the other hand for Reynolds number close
593 to the critical Reynolds number, there is a prolonged, unsteady, elongation
594 period, in which periodic motion is observed and the deformation parameter
595 D is close to one. The “vacillating” behavior cannot last forever, ultimately
596 (perhaps stochastically!), the bubble will either settle down or break. We assert
597 that regardless of the outcome, this vacillating behaviour will always occur in
598 close proximity to the critical Reynolds’ number. In other words, regardless of
599 the outcome, we claim, using the grid resolution of $R/16$, that one is assured
600 of being within 3 percent of the critical Reynolds number (see Figure 3). In
601 fact, we hypothesize that there will always be “vacillating” behavior if one is
602 sufficiently close to the critical Reynolds number. i.e. given an almost infinite
603 supply of computational resources, as one hones in closer and closer to the
604 critical Reynolds number, a “tug of war” will be observed between the surface
605 tension force trying to pull the bubble together versus the wall driven shear
606 stress trying to pull the bubble apart.

607 4.4. Velocity field outside and inside the breaking bubble

608 In this section, we consider the fluid flow velocity field outside and inside the
609 bubble during the shear-induced breakup process. **Detailed velocity fields of the**
610 **deforming and breaking drop have already been presented in some references**
611 **(Li et al. [33], Renardy and Cristini [47]).** The velocity fields for the drop and
612 the bubble will be influenced by the behavior of the breakup process, so the
613 velocity fields for the drop and the bubble are not similar. Figure 9 shows the

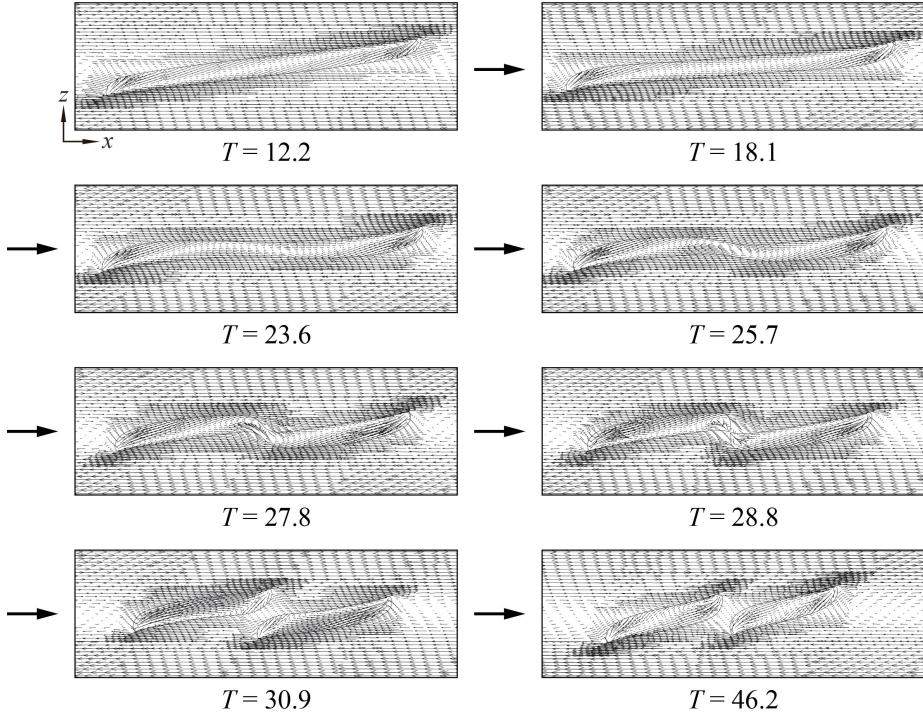


Figure 9: Fluid velocity field outside and inside the breaking bubble in shear flow at the condition $Ca = 0.3$ and $Re = 93$. The “bubble” critical Reynolds number corresponding to $Ca = 0.3$ is $92 < Re_c < 93$. ($\lambda = 1.2 \times 10^{-3}$, $\eta < 1.0 \times 10^{-3}$)

velocity fields outside and inside the bubble at cross-sectional slices in the xz -plane for a flow condition of $Ca = 0.3$ and $Re = 93$. Regions around the bubble where there is a higher density of velocity vectors correspond to the level-1 grid portion of the AMR structure. The simulation results show that the velocity field inside the bubble is particularly distinct from the surrounding flow field in the exterior of the bubble. The cross-sections at $T = 12.2$ and $T = 18.1$, taken during the elongation phase, show how shear forces at the lower and upper halves of the bubble act along the bottom and top surfaces, respectively, to deform the interface. Near the left and right edges of the bubble, inward interior flows (that point toward the bubble center) begin to develop. Strong shearing forces in the exterior near the bottom-left-end and top-right-end of the bubble interact with the interior flow field through the boundary to create cusped shapes at the bottom-left and top-right ends of the bubble while the interface is laterally elongated in the x -direction. During the shrinking process, which occurs for $23.6 \leq T \leq 27.8$, inward flows within the bubble extend over a wider region and are no longer localized near the bubble edges. Then, we observe that circulating flows form at the thread-bridge part of the doglegged bubble shape over the time interval $[25.7, 27.8]$. During the breakup process

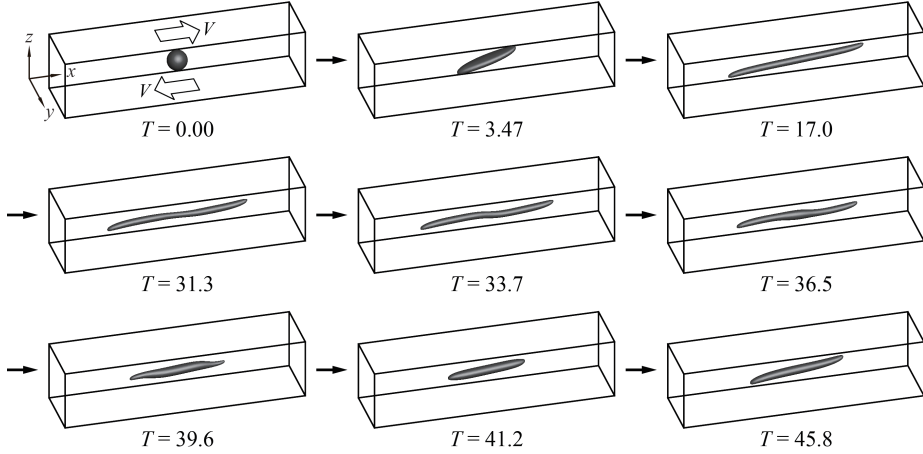


Figure 10: Time evolution of bubble deformation in shear flow at the condition of $Ca = 0.8$ and $Re = 42$. The “bubble” critical Reynolds number corresponding to $Ca = 0.8$ is $42 < Re_c < 43$. ($\lambda = 1.2 \times 10^{-3}$, $\eta < 1.0 \times 10^{-3}$)

($T \sim 28.8$), higher-intensity inward flows are formed inside the bubble, near the pinch off region, that are naturally larger than the surrounding interior flows and which are inextricably associated with the bubble migration illustrated in Figs. 6 and 7. As time proceeds further ($T = 46.2$), distinct inward flows are formed inside the daughter bubbles; the bubbles then begin their migration toward the side walls. Considering the left daughter bubble, for example, we see that the mechanism responsible for this movement results from larger shear forces acting on the bottom-left end than those in the top-left end.

4.5. Effect of surface tension on bubble deformation and breakup

In previous sections, we considered numerical simulations of bubble deformation and breakup with a capillary number $Ca = 0.3$. Here, we examine similar bubble dynamics with $Ca = 0.8$ and we also investigate the effect of interfacial tension on bubble deformation and breakup. Using $Ca = 0.8$ for both cases, Figures 10 and 11 present the time evolution of shear-induced bubble deformation and breakup with $Re = 42$ and $Re = 43$, respectively. We note that the bubble critical Reynolds number is around $Re_c \approx 43$, whereas $Re_c \approx 0$ for the corresponding case of the drop with $\lambda = \eta = 1$ (see e.g. Li et al. [33]). Note that Re_c for $Ca = 0.8$ is smaller than that for the condition of $Ca = 0.3$ since the bubble at $Ca = 0.8$ is more elastic due to the weaker effect of surface tension in this case. The results shown in Figs. 10 and 11 indicate that the bubble deformation and breakup process for the condition of $Ca = 0.8$ is analogous to that for $Ca = 0.3$. For the case of bubble deformation without breakup (Fig. 10), the bubble initially assumes a long elongated shape along the x -direction at around $T = 17.0$. The bubble then enters a compression stage over the time interval $[31.3, 41.2]$ and subsequently starts to elongate again at

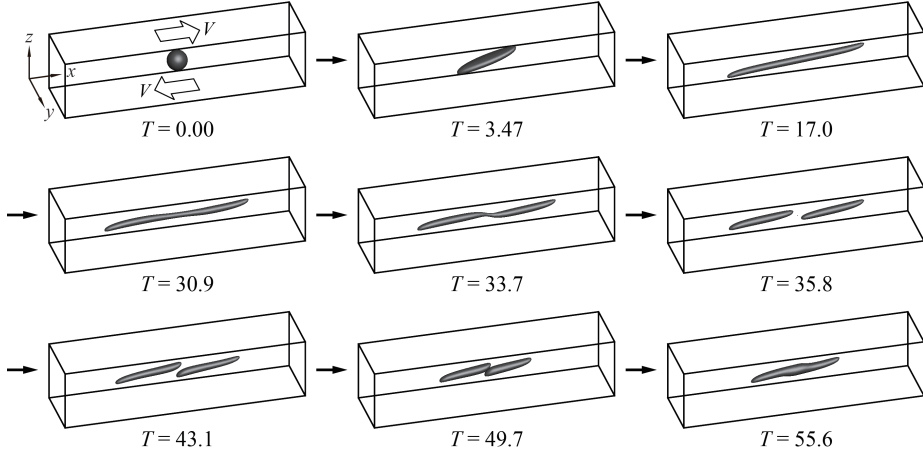


Figure 11: Time evolution of bubble deformation in shear flow at the condition of $Ca = 0.8$ and $Re = 43$. The “bubble” critical Reynolds number corresponding to $Ca = 0.8$ is $42 < Re_c < 43$. ($\lambda = 1.2 \times 10^{-3}$, $\eta < 1.0 \times 10^{-3}$)

657 $T = 45.8$. On the other hand, for the case of bubble breakup (Fig. 11), an
 658 initial elongation phase is followed by a doglegged shape formation at $T = 33.7$.
 659 After that, the bubble ruptures from the thread-bridge part of the doglegged
 660 shape and two daughter bubbles are produced ($T = 35.8$). The two daughter
 661 bubbles formed after breakup move to the central area ($T = 49.7$) as in the case
 662 of $Ca = 0.8$ and $Re = 93$, but the two bubbles eventually coalesce in a region
 663 approximately centered in the computational domain ($T = 55.6$). We note that
 664 in a real experimental setting, bubbles may coalesce after breaking up due to
 665 slight deviations of flow conditions and states. Although the process of bubble
 666 deformation and breakup for flow conditions with $Ca = 0.3$ and $Ca = 0.8$ are
 667 similar, a pronounced difference is that the bubble for $Ca = 0.8$ is more elon-
 668 gated and slender than that for $Ca = 0.3$ due to the smaller effect of surface
 669 tension for $Ca = 0.8$.

670 Table 4 lists, for representative Ca values, the corresponding critical Reynolds
 671 number, Re_c , for shear-induced bubble breakup. The data in Table 4 corre-
 672 sponds to $\lambda = 1.2 \times 10^{-3}$, $\eta < 1.0 \times 10^{-3}$, $0.3 < Ca < 1$, and the initial/boundary
 673 conditions are given by (1). The results in Table 4 indicate that sufficiently large
 674 shear forces are required for bubble breakup even for large capillary numbers.
 675 In Figure 12 we plot the smooth interpolant of the data given in Table 4 and
 676 make the hypothesis that given a new data point, (Ca, Re) , shear induced bub-
 677 ble break up will occur if the point (Ca, Re) is above the given critical curve,
 678 and the bubble will not break if the (Ca, Re) pair is below the critical curve.
 679 For comparison, a critical curve for the drop with $\lambda = \eta = 1$ is also indicated
 680 in Fig. 12. The inclusion of breakup and no-breakup critical curves, for both
 681 the drop and the bubble, will facilitate future identification of Re_c numbers—
 682 and thus a more complete general critical curve—for a wide range of high Ca

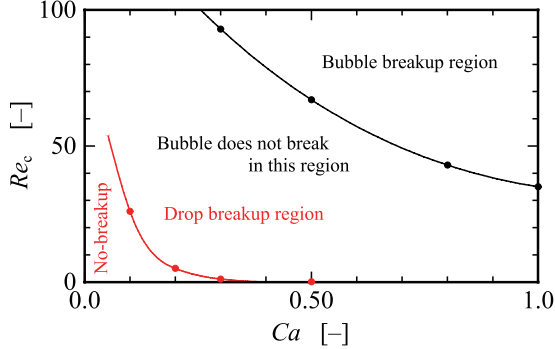


Figure 12: A plot of the critical Reynolds number versus capillary number for the data listed in Table 4. $\lambda = 1.2 \times 10^{-3}$, $\eta < 1.0 \times 10^{-3}$, $0.3 < Ca < 1$, and the initial/boundary conditions are given by (1). Given a new data point, (Ca, Re) , one can reliably predict whether the given (Ca, Re) pair will result in shear induced bubble break-up or not. Note, for the “Drop delineation curve,” $\lambda = \eta = 1$.

683 numbers.

Table 4: Shear-induced bubble breakup for various flow conditions described in terms of column pairs of critical Reynolds numbers and corresponding capillary numbers. ($\lambda = 1.2 \times 10^{-3}$, $\eta < 1.0 \times 10^{-3}$)

Capillary number Ca	0.3	0.5	0.8	1.0
Critical Reynolds number Re_c	93	67	43	35

684 5. Conclusions

685 The bubble deformation and breakup process in liquid due to a driving
 686 simple linear shear flow was explored numerically using the CLSVOF compu-
 687 tational method. In this study, the critical Reynolds number Re_c , at which
 688 bubble breakup first occurs, was determined for several flow conditions, and the
 689 differences between the morphology of bubble deformation and breakup were
 690 compared with the analogous morphology of drop deformation and breakup.

691 The numerical results revealed significant differences between bubble de-
 692 formation and breakup and the corresponding drop dynamics. For the case of a
 693 bubble, it was discovered that much stronger shear flows are necessary in order
 694 to induce interface breakup compared with a drop immersed in a similar flow
 695 field. That is, a much larger Reynolds number flow is required in order to induce
 696 bubble breakup. The steps leading to bubble breakup were similar throughout
 697 the Ca number range considered in our computations: the bubble underwent a
 698 similar breakup mechanism in which rupture occurred at a thread-bridge part
 699 that followed a doglegged shape formation stage. For bubble deformation with-
 700 out breakup, near Re_c , the bubble did not maintain a stable deformed shape,

701 in contrast to drop deformation near the critical Reynolds number. The bubble
702 exhibited pronounced underdamped behavior: the bubble oscillated between
703 elongating and shrinking motions for non-rupturing flow conditions. At the
704 same time, bubble deformation under smaller Re conditions ($< Re_c$) led to a
705 stable state. We attribute the large differences in morphology for the bubble
706 undergoing breakup, compared with the drop, due to the density and viscosity
707 ratio.

708 There are a number of directions for future work. In the present work, we
709 varied the Capillary number and Reynolds' number in studying bubble defor-
710 mation and breakup morphology in the presence of a simple shear flow. For
711 the future, one can also vary (i) the viscosity ratio, (ii) the effect of the initial
712 shape of the bubble[39], (iii) the magnitude and direction of the gravitational
713 force, (iv) the non-Newtonian properties of the “matrix” liquid, (v) bubble de-
714 formation and breakup due to a shear flow in a T junction[16], (vi) bubble de-
715 formation and breakup confined shear flow (see [18] for the drop case), and
716 (vii) bubble deformation and breakup due to non-uniform shear flow (see [6] for
717 the drop case).

718 References

- 719 [1] Amani, A., Balcázar, N., Castro, J., Oliva, A., 2019. Numerical study of droplet deformation in shear flow using a con-
720 servative level-set method. Chemical Engineering Science 207,
721 153–171. URL: <http://www.sciencedirect.com/science/article/pii/S0009250919305123>, doi:<https://doi.org/10.1016/j.ces.2019.06.014>.
- 725 [2] Arienti, M., Li, X., Soteriou, M., Eckett, C., Sussman, M., Jensen, R., 2013. Coupled level-set/volume-of-fluid method for simulation of injector
726 atomization. Journal of propulsion and power 29, 147–157.
- 728 [3] Bazhlekov, I.B., Anderson, P.D., Meijer, H.E., 2006. Numerical investi-
729 gation of the effect of insoluble surfactants on drop deformation and
730 breakup in simple shear flow. Journal of Colloid and Interface Sci-
731 ence 298, 369 – 394. URL: <http://www.sciencedirect.com/science/article/pii/S0021979705012658>, doi:<http://dx.doi.org/10.1016/j.jcis.2005.12.017>.
- 734 [4] Bento, D., Rodrigues, R.O., Faustino, V., Pinho, D., Fernandes, C.S.,
735 Pereira, A.I., Garcia, V., Miranda, J.M., Lima, R., 2018. Deforma-
736 tion of red blood cells, air bubbles, and droplets in microfluidic devices:
737 Flow visualizations and measurements. Micromachines 9, 151. URL:
738 <https://www.mdpi.com/2072-666X/9/4/151>, doi:10.3390/mi9040151.
- 739 [5] Canedo, E.L., Favelukis, M., Tadmor, Z., Talmon, Y., 1993.
740 An experimental study of bubble deformation in viscous liq-
741 uids in simple shear flow. AIChE Journal 39, 553–559. URL:

- 742 <https://aiche.onlinelibrary.wiley.com/doi/abs/10.1002/aic.690390403>, doi:<https://doi.org/10.1002/aic.690390403>,
 743 arXiv:<https://aiche.onlinelibrary.wiley.com/doi/pdf/10.1002/aic.690390403>.
- 744
- 745 [6] Chin, H.B., Han, C.D., 1980. Studies on droplet deformation and breakup.
 746 ii. breakup of a droplet in nonuniform shear flow. *Journal of rheology* 24,
 747 1–37.
- 748 [7] Chu, P., Finch, J., Bournival, G., Ata, S., Hamlett, C., Pugh, R.J.,
 749 2019. A review of bubble break-up. *Advances in Colloid and In-*
 750 *terface Science* 270, 108–122. URL: <https://www.sciencedirect.com/science/article/pii/S0001868619300211>, doi:<https://doi.org/10.1016/j.cis.2019.05.010>.
- 751
- 752 [8] Cristini, V., Bławzdziewicz, J., Loewenberg, M., 2001. An adap-
 753 tive mesh algorithm for evolving surfaces: simulations of drop breakup
 754 and coalescence. *Journal of Computational Physics* 168, 445 –
 755 463. URL: <http://www.sciencedirect.com/science/article/pii/S0021999101967130>, doi:<http://dx.doi.org/10.1006/jcph.2001.6713>.
- 756
- 757 [9] Cristini, V., Guido, S., Alfani, A., Bławzdziewicz, J., Loewenberg, M.,
 758 2003. Drop breakup and fragment size distribution in shear flow. *Journal*
 759 *of Rheology* 47, 1283–1298. URL: <http://scitation.aip.org/content/sor/journal/jor2/47/5/10.1122/1.1603240>, doi:<http://dx.doi.org/10.1122/1.1603240>.
- 760
- 761 [10] Croce, R., Griebel, M., Schweitzer, M.A., 2010. Numerical simulation of
 762 bubble and droplet deformation by a level set approach with surface tension
 763 in three dimensions. *International Journal for Numerical Methods in Fluids*
 764 62, 963–993. URL: <http://dx.doi.org/10.1002/fld.2051>, doi:<10.1002/fld.2051>.
- 765
- 766 [11] Drenckhan, W., Saint-Jalmes, A., 2015. The science of foaming. *Ad-*
 767 *vances in Colloid and Interface Science* 222, 228–259. URL: <https://www.sciencedirect.com/science/article/pii/S0001868615000603>,
 768 doi:<https://doi.org/10.1016/j.cis.2015.04.001>. Reinhard Miller,
 769 Honorary Issue.
- 770
- 771 [12] Eftekhari, M., Schwarzenberger, K., Heitkam, S., Eckert, K.,
 772 2021a. Interfacial flow of a surfactant-laden interface under asym-
 773 metric shear flow. *Journal of Colloid and Interface Science* 599,
 774 837–848. URL: <https://www.sciencedirect.com/science/article/pii/S0021979721006457>, doi:<https://doi.org/10.1016/j.jcis.2021.04.126>.
- 775
- 776 [13] Eftekhari, M., Schwarzenberger, K., Heitkam, S., Javadi, A.,
 777 Bashkatov, A., Ata, S., Eckert, K., 2021b. Interfacial be-
 778 havior of particle-laden bubbles under asymmetric shear flow.
 779 *Langmuir* 37, 13244–13254. URL: <https://doi.org/10.1021/acs.langmuir.1c02544>.
- 780
- 781
- 782

- 783 acs.langmuir.1c01814, doi:10.1021/acs.langmuir.1c01814,
 784 arXiv:<https://doi.org/10.1021/acs.langmuir.1c01814>. pMID:
 785 34726918.
- 786 [14] Ervin, E., Tryggvason, G., 1997. The rise of bubbles in a vertical shear
 787 flow. Journal of Fluids Engineering 119(2), 443–449.
- 788 [15] Fang, Z., Shuai, Y., Huang, Z., Wang, J., Yang, Y., 2024. Inten-
 789 sification of polyethylene devolatilization in twin-screw extruder
 790 with additives. Polymer Engineering & Science 64, 2961–2974.
 791 URL: <https://4sceppublications.onlinelibrary.wiley.com/doi/abs/10.1002/pen.26738>, doi:<https://doi.org/10.1002/pen.26738>,
 792 arXiv:<https://4sceppublications.onlinelibrary.wiley.com/doi/pdf/10.1002/pen.26738>.
- 793 [16] Frense, E., Rüdiger, F., Fröhlich, J., 2024. Modeling of dynamic bub-
 794 ble deformation and breakup in t-junction channel flow. Chemical En-
 795 gineering Science 300, 120579. URL: <https://www.sciencedirect.com/science/article/pii/S0009250924008790>, doi:<https://doi.org/10.1016/j.ces.2024.120579>.
- 795 [17] Gao, S., Shi, Y., Pan, G., Quan, X., 2022. Research on the
 796 effect of asymmetric bubbles on the load characteristics of projec-
 797 tiles during an underwater salvo. Applied Ocean Research 124,
 798 103212. URL: <https://www.sciencedirect.com/science/article/pii/S0141118722001535>, doi:<https://doi.org/10.1016/j.apor.2022.103212>.
- 800 [18] Gupta, A., Sbragaglia, M., 2014. Deformation and breakup of viscoelastic
 801 droplets in confined shear flow. Physical Review E 90, 023305.
- 802 [19] Hernandez, F.H., Rangel, R.H., 2017. Breakup of drops in simple
 803 shear flows with high-confinement geometry. Computers & Fluids 146,
 804 23 – 41. URL: <http://www.sciencedirect.com/science/article/pii/S0045793017300038>, doi:<https://doi.org/10.1016/j.compfluid.2017.01.001>.
- 805 [20] Hirt, C., Nichols, B., 1981. Volume of fluid (vof) method
 806 for the dynamics of free boundaries. Journal of Computational
 807 Physics 39, 201 – 225. URL: <http://www.sciencedirect.com/science/article/pii/0021999181901455>, doi:[http://dx.doi.org/10.1016/0021-9991\(81\)90145-5](http://dx.doi.org/10.1016/0021-9991(81)90145-5).
- 810 [21] Hoyt, N.C., 2013. The performance of passive cyclonic separators in mi-
 811 crogravity. Case Western Reserve University.
- 812 [22] Inamuro, T., 2006. Lattice boltzmann methods for viscous fluid flows and
 813 for two-phase fluid flows. Fluid Dynamics Research 38, 641. URL: <http://stacks.iop.org/1873-7005/38/i=9/a=A04>.

- 822 [23] Inamuro, T., Tomita, R., Ogino, F., 2003. Lattice boltzmann simu-
823 lations of drop deformation and breakup in simple shear flows. International Journal of Modern Physics B 17, 21–26. URL: <http://www.worldscientific.com/doi/abs/10.1142/S0217979203017035>, doi:10.
824 1142/S0217979203017035.
- 827 [24] Ioannou, N., Liu, H., Zhang, Y., 2016. Droplet dynamics
828 in confinement. Journal of Computational Science 17, 463 –
829 474. URL: <http://www.sciencedirect.com/science/article/pii/S1877750316300308>, doi:<https://doi.org/10.1016/j.jocs.2016.03.009>. discrete Simulation of Fluid Dynamics 2015.
- 832 [25] Janssen, P., Anderson, P., 2008. A boundary-integral model for
833 drop deformation between two parallel plates with non-unit viscosity
834 ratio drops. Journal of Computational Physics 227, 8807–
835 8819. URL: <http://www.sciencedirect.com/science/article/pii/S002199910800346X>, doi:<http://dx.doi.org/10.1016/j.jcp.2008.06.027>.
- 838 [26] Janssen, P.J.A., Anderson, P.D., 2007. Boundary-integral method
839 for drop deformation between parallel plates. Physics of Fluids
840 19. URL: <http://scitation.aip.org/content/aip/journal/pof2/19/4/10.1063/1.2715621>, doi:<http://dx.doi.org/10.1063/1.2715621>.
- 842 [27] Kang, M., Fedkiw, R.P., Liu, X.D., 2000. A boundary condition capturing
843 method for multiphase incompressible flow. Journal of scientific computing
844 15, 323–360.
- 845 [28] Khismatullin, D.B., Renardy, Y., Cristini, V., 2003. Inertia-induced
846 breakup of highly viscous drops subjected to simple shear. Physics of Fluids
847 15, 1351–1354. doi:<http://dx.doi.org/10.1063/1.1564825>.
- 848 [29] Komrakova, A., Shardt, O., Eskin, D., Derksen, J., 2014. Lattice
849 boltzmann simulations of drop deformation and breakup in shear flow.
850 International Journal of Multiphase Flow 59, 24 – 43. URL: <http://www.sciencedirect.com/science/article/pii/S0301932213001547>,
851 doi:<http://dx.doi.org/10.1016/j.ijmultiphaseflow.2013.10.009>.
- 853 [30] Komrakova, A., Shardt, O., Eskin, D., Derksen, J., 2015. Ef-
854 fects of dispersed phase viscosity on drop deformation and breakup
855 in inertial shear flow. Chemical Engineering Science 126, 150 –
856 159. URL: <http://www.sciencedirect.com/science/article/pii/S000925091400726X>, doi:<http://dx.doi.org/10.1016/j.ces.2014.12.012>.
- 859 [31] Legendre, D., Magnaudet, J., 1998. The lift force on a spherical bubble in
860 a viscous linear shear flow. Journal of Fluid Mechanics 368, 81–126.

- 861 [32] Lewin-Jones, P., Lockerby, D.A., Sprittles, J.E., 2024. Collision of liquid
862 drops: bounce or merge? *Journal of Fluid Mechanics* 995, A1. doi:10.
863 1017/jfm.2024.722.
- 864 [33] Li, J., Renardy, Y., Renardy, M., 2000. Numerical simulation of
865 breakup of a viscous drop in simple shear flow through a volume-of-fluid
866 method. *Physics of Fluids* 12, 269–282. URL: <http://scitation.aip.org/content/aip/journal/pof2/12/2/10.1063/1.870305>, doi:<http://dx.doi.org/10.1063/1.870305>.
- 869 [34] Li, X., Soteriou, M.C., 2016. High fidelity simulation and analysis of liq-
870 uid jet atomization in a gaseous crossflow at intermediate weber numbers.
871 *Physics of Fluids* 28.
- 872 [35] Lohse, D., 2018. Bubble puzzles: from fundamentals to applications. *Phys-
873 ical review fluids* 3, 110504.
- 874 [36] Müller-Fischer, N., Tobler, P., Dressler, M., Fischer, P., Windhab, E.J.,
875 2008. Single bubble deformation and breakup in simple shear flow. *Experi-
876 ments in fluids* 45, 917–926.
- 877 [37] Ohta, M., Akama, Y., Yoshida, Y., Sussman, M., 2014. Influence of the
878 viscosity ratio on drop dynamics and breakup for a drop rising in an im-
879 miscible low-viscosity liquid. *Journal of Fluid Mechanics* 752, 383–409.
880 doi:10.1017/jfm.2014.339.
- 881 [38] Ohta, M., Furukawa, T., Yoshida, Y., Sussman, M., 2019. A
882 three-dimensional numerical study on the dynamics and deformation
883 of a bubble rising in a hybrid carreau and fene-cr modeled poly-
884 meric liquid. *Journal of Non-Newtonian Fluid Mechanics* 265, 66–
885 78. URL: <https://www.sciencedirect.com/science/article/pii/S0377025718301952>, doi:<https://doi.org/10.1016/j.jnnfm.2018.12.012>.
- 888 [39] Ohta, M., Imura, T., Yoshida, Y., Sussman, M., 2005. A computational
889 study of the effect of initial bubble conditions on the motion of a gas bubble
890 rising in viscous liquids. *International journal of multiphase flow* 31, 223–
891 237.
- 892 [40] Ohta, M., Kikuchi, D., Yoshida, Y., Sussman, M., 2011. Robust numeri-
893 cal analysis of the dynamic bubble formation process in a viscous liquid.
894 *International Journal of Multiphase Flow* 37, 1059–1071.
- 895 [41] Ohta, M., Sussman, M., 2012. The buoyancy-driven mo-
896 tion of a single skirted bubble or drop rising through
897 a viscous liquid. *Physics of Fluids* 24, 112101. URL:
898 <https://doi.org/10.1063/1.4765669>, doi:10.1063/1.4765669,
899 arXiv:https://pubs.aip.org/aip/pof/article-pdf/doi/10.1063/1.4765669/14128560/112101_1_o

- 900 [42] Ohta, M., Yamaguchi, S., Yoshida, Y., Sussman, M., 2010. The sensitivity
901 of drop motion due to the density and viscosity ratio. Physics of Fluids 22.
- 902 [43] Rallison, J.M., 1984. The deformation of small viscous drops
903 and bubbles in shear flows. Annual Review of Fluid Mechanics 16, 45–66.
904 URL: <http://dx.doi.org/10.1146/annurev.fl.16.010184.000401>,
905 doi:10.1146/annurev.fl.16.010184.000401,
906 arXiv:<http://dx.doi.org/10.1146/annurev.fl.16.010184.000401>.
- 907 [44] Renardy, Y., 2006. Numerical simulation of a drop undergoing large am-
908 plitude oscillatory shear. Rheologica acta 45, 223–227.
- 909 [45] Renardy, Y., 2007. The effects of confinement and inertia on the production
910 of droplets. Rheologica Acta 46, 521–529. URL: <http://dx.doi.org/10.1007/s00397-006-0150-y>,
911 doi:10.1007/s00397-006-0150-y.
- 912 [46] Renardy, Y., 2008. Effect of startup conditions on drop breakup under
913 shear with inertia. International Journal of Multiphase Flow 34, 1185 – 1189.
914 URL: <http://www.sciencedirect.com/science/article/pii/S030193220800089X>,
915 doi:<http://dx.doi.org/10.1016/j.ijmultiphaseflow.2008.04.004>.
- 916 [47] Renardy, Y., Cristini, V., 2001a. Effect of inertia on drop breakup under
917 shear. Physics of Fluids 13, 7–13. URL: <http://scitation.aip.org/content/aip/journal/pof2/13/1/10.1063/1.1331321>,
918 doi:<http://dx.doi.org/10.1063/1.1331321>.
- 919 [48] Renardy, Y., Cristini, V., Li, J., 2002. Drop fragment distributions un-
920 der shear with inertia. International Journal of Multiphase Flow 28, 1125
921 – 1147. URL: <http://www.sciencedirect.com/science/article/pii/S0301932202000228>,
922 doi:[http://dx.doi.org/10.1016/S0301-9322\(02\)00022-8](http://dx.doi.org/10.1016/S0301-9322(02)00022-8).
- 923 [49] Renardy, Y.Y., Cristini, V., 2001b. Scalings for fragments produced
924 from drop breakup in shear flow with inertia. Physics of Fluids 13,
925 2161–2164. URL: <https://doi.org/10.1063/1.1384469>,
926 doi:10.1063/1.1384469, arXiv:<https://doi.org/10.1063/1.1384469>.
- 927 [50] Rust, A., Manga, M., 2002. Bubble shapes and orientations in low re-
928 simple shear flow. Journal of Colloid and Interface Science 249, 476–
929 480. URL: <https://www.sciencedirect.com/science/article/pii/S0021979702982925>,
doi:<https://doi.org/10.1006/jcis.2002.8292>.
- 930 [51] Sanogo, B., Souidi, K., Marcatti, A., Vial, C., 2023. Food aeration: Ef-
931 fect of the surface-active agent type on bubble deformation and break-up
932 in a viscous newtonian fluid: From single bubble to process-scale. Food
933 Research International 165, 112478. URL: <https://www.sciencedirect.com/science/article/pii/S0963996923000236>,
934 doi:<https://doi.org/10.1016/j.foodres.2023.112478>.

- 940 [52] Schlüter, M., Herres-Pawlis, S., Nieken, U., Tuttles, U., Bothe, D., 2021.
 941 Small-scale phenomena in reactive bubbly flows: Experiments, numerical
 942 modeling, and applications. Annual review of chemical and biomolecular
 943 engineering 12, 625–643.
- 944 [53] Sharifi, R., Varmazyar, M., Mohammadi, A., 2024. Investigating
 945 droplet and bubble deformation under shear flow using the multi-pseudo-potential
 946 scheme of lattice boltzmann method. Advances in Applied Mathematics and Mechanics
 947 16, 519–548. URL: <https://global-sci.com/article/72820/investigating-droplet-and-bubble-deformation-under-shear-flow-using-the-multi-pseudo-potential-scheme-of-lattice-boltzmann-method>.
 948 doi:<https://doi.org/10.4208/aamm.OA-2021-0326>.
- 951 [54] Sines, J.N., Straiton, B.J., Zuccarelli, C.E., Marashdeh, Q.M., Teixeira,
 952 F.L., Fan, L.S., Motil, B.J., 2020. Study of gas-water flow inside
 953 of a horizontal passive cyclonic gas-liquid phase separator system using
 954 displacement-current phase tomography. Gravitational and Space Research
 955 6, 28–43.
- 956 [55] Stewart, P., Lay, N., Sussman, M., Ohta, M., 2008. An improved sharp
 957 interface method for viscoelastic and viscous two-phase flows. Journal of
 958 Scientific Computing 35, 43–61.
- 959 [56] Stone, H.A., 1994. Dynamics of drop deformation and breakup
 960 in viscous fluids. Annual Review of Fluid Mechanics 26,
 961 65–102. URL: <http://dx.doi.org/10.1146/annurev.fl.26.010194.000433>,
 962 doi:<https://doi.org/10.1146/annurev.fl.26.010194.000433>.
 963 arXiv:<http://dx.doi.org/10.1146/annurev.fl.26.010194.000433>.
- 964 [57] Sussman, M., 2003. A second order coupled level set and volume-
 965 of-fluid method for computing growth and collapse of vapor bubbles. Journal of Computational Physics 187, 110–136. URL: <https://www.sciencedirect.com/science/article/pii/S0021999103000871>,
 966 doi:[https://doi.org/10.1016/S0021-9991\(03\)00087-1](https://doi.org/10.1016/S0021-9991(03)00087-1).
- 969 [58] Sussman, M., Almgren, A.S., Bell, J.B., Colella, P., Howell, L.H.,
 970 Welcome, M.L., 1999. An adaptive level set approach for incom-
 971 pressible two-phase flows. Journal of Computational Physics 148, 81
 972 – 124. URL: <http://www.sciencedirect.com/science/article/pii/S002199919896106X>, doi:<https://doi.org/10.1006/jcph.1998.6106>.
- 974 [59] Sussman, M., Puckett, E.G., 2000. A coupled level set and
 975 volume-of-fluid method for computing 3d and axisymmetric incompress-
 976 ible two-phase flows. Journal of Computational Physics 162, 301–
 977 337. URL: <http://www.sciencedirect.com/science/article/pii/S0021999100965379>, doi:<http://dx.doi.org/10.1006/jcph.2000.6537>.
- 979 [60] Sussman, M., Smereka, P., Osher, S., 1994. A level set ap-
 980 proach for computing solutions to incompressible two-phase flow.

- 981 Journal of Computational Physics 114, 146 – 159. URL: <http://www.sciencedirect.com/science/article/pii/S0021999184711557>,
 982 doi:<http://dx.doi.org/10.1006/jcph.1994.1155>.
- 984 [61] Sussman, M., Smith, K., Hussaini, M., Ohta, M., Zhi-Wei, R., 2007. A
 985 sharp interface method for incompressible two-phase flows. Journal of Com-
 986 putational Physics 221, 469–505. URL: <https://www.sciencedirect.com/science/article/pii/S0021999106002981>, doi:<https://doi.org/10.1016/j.jcp.2006.06.020>.
- 989 [62] Tanguy, S., Ménard, T., Berlemont, A., 2007. A level set method for
 990 vaporizing two-phase flows. Journal of Computational Physics 221, 837–
 991 853.
- 992 [63] Tatebe, O., 1993. The multigrid preconditioned conjugate gradient method,
 993 in: NASA. Langley Research Center, The Sixth Copper Mountain Confer-
 994 ence on Multigrid Methods, Part 2.
- 995 [64] Taylor, G.I., 1932. The viscosity of a fluid containing small drops of another
 996 fluid. Proceedings of the Royal Society of London A: Mathematical, Phys-
 997 ical and Engineering Sciences 138, 41–48. doi:[10.1098/rspa.1932.0169](https://doi.org/10.1098/rspa.1932.0169).
- 998 [65] Taylor, G.I., 1934. The formation of emulsions in definable fields of flow.
 999 Proceedings of the Royal Society of London A: Mathematical, Physical and
 1000 Engineering Sciences 146, 501–523. doi:[10.1098/rspa.1934.0169](https://doi.org/10.1098/rspa.1934.0169).
- 1001 [66] Unverdi, S.O., Tryggvason, G., 1992. A front-tracking method
 1002 for viscous, incompressible, multi-fluid flows. Journal of Compu-
 1003 tational Physics 100, 25 – 37. URL: <http://www.sciencedirect.com/science/article/pii/002199919290307K>, doi:[http://dx.doi.org/10.1016/0021-9991\(92\)90307-K](http://dx.doi.org/10.1016/0021-9991(92)90307-K).
- 1006 [67] Wang, A., Evans, G., Mitra, S., 2023. A review of bubble
 1007 surface loading and its effect on bubble dynamics. Minerals
 1008 Engineering 199, 108105. URL: <https://www.sciencedirect.com/science/article/pii/S089268752300119X>, doi:<https://doi.org/10.1016/j.mineng.2023.108105>.
- 1011 [68] Wang, Z., Shi, D., Zhang, A., 2015. Three-dimensional lattice boltz-
 1012 mann simulation of bubble behavior in a flap-induced shear flow. Com-
 1013 puters & Fluids 123, 44 – 53. URL: <http://www.sciencedirect.com/science/article/pii/S0045793015003199>, doi:<https://doi.org/10.1016/j.compfluid.2015.09.007>.
- 1016 [69] Wei, Y.K., Qian, Y., Xu, H., 2012. Lattice boltzmann simulations
 1017 of single bubble deformation and breakup in a shear flow. The Jour-
 1018 nal of Computational Multiphase Flows 4, 111–117. URL: <https://doi.org/10.1260/1757-482X.4.1.111>, doi:[10.1260/1757-482X.4.1.111](https://doi.org/10.1260/1757-482X.4.1.111), arXiv:<https://doi.org/10.1260/1757-482X.4.1.111>.

- 1021 [70] Wong, A., Park, C., 2012. A visualization system for observing
 1022 plastic foaming processes under shear stress. *Polymer Testing*
 1023 31, 417–424. URL: <https://www.sciencedirect.com/science/article/pii/S0142941811002169>, doi:<https://doi.org/10.1016/j.polymertesting.2011.12.012>.
- 1026 [71] Yoshikawa, H.N., Zoueshtiagh, F., Caps, H., Kurowski, P., Petitjeans, P.,
 1027 2010. Bubble splitting in oscillatory flows on ground and in reduced gravity.
 1028 *The European Physical Journal E* 31, 191–199.
- 1029 [72] Zhang, J., Miksis, M.J., Bankoff, S.G., 2006. Nonlinear dynamics of
 1030 a two-dimensional viscous drop under shear flow. *Physics of Fluids*
 1031 18. URL: <http://scitation.aip.org/content/aip/journal/pof2/18/7/10.1063/1.2222336>, doi:<http://dx.doi.org/10.1063/1.2222336>.
- 1033 [73] Zhang, J., Ni, M.J., Magnaudet, J., 2021a. Three-dimensional dynamics
 1034 of a pair of deformable bubbles rising initially in line. part 1. moderately
 1035 inertial regimes. *Journal of Fluid Mechanics* 920, A16.
- 1036 [74] Zhang, J., Ni, M.J., Magnaudet, J., 2022. Three-dimensional dynamics of
 1037 a pair of deformable bubbles rising initially in line. part 2. highly inertial
 1038 regimes. *Journal of Fluid Mechanics* 943, A10.
- 1039 [75] Zhang, J., Shu, S., Guan, X., Yang, N., 2021b. Regime map-
 1040 ping of multiple breakup of droplets in shear flow by phase-field
 1041 lattice boltzmann simulation. *Chemical Engineering Science* 240,
 1042 116673. URL: <https://www.sciencedirect.com/science/article/pii/S0009250921002384>, doi:<https://doi.org/10.1016/j.ces.2021.116673>.
- 1045 [76] Zhang, W., Almgren, A., Beckner, V., Bell, J., Blaschke, J., Chan, C.,
 1046 Day, M., Friesen, B., Gott, K., Graves, D., Katz, M., Myers, A., Nguyen,
 1047 T., Nonaka, A., Rosso, M., Williams, S., Zingale, M., 2019. AMReX: a
 1048 framework for block-structured adaptive mesh refinement. *Journal of Open
 1049 Source Software* 4, 1370. URL: <https://doi.org/10.21105/joss.01370>,
 1050 doi:[10.21105/joss.01370](https://doi.org/10.21105/joss.01370).